5-2013

Synthesis of Optimized InP/ZnS Core/Shell Nanocrystals and TiO2 Nanotubes for Quantum Dot Sensitized Solar Cells

Seungyong Lee
University of Arkansas, Fayetteville

SYNTHESIS OF OPTIMIZED InP/ZnS CORE/SHELL NANOCRYSTALS AND TiO_2 NANOTUBES FOR QUANTUM DOT SENSITIZED SOLAR CELLS

SYNTHESIS OF OPTIMIZED InP/ZnS CORE/SHELL NANOCRYSTALS AND TiO_2 NANOTUBES FOR QUANTUM DOT SENSITIZED SOLAR CELLS

A thesis submitted in partial fulfillment
of the requirements for the degree of
Master of Science in Electrical Engineering

By

Seungyong Lee
Sogang University
Bachelor of Engineering in Electronics and Chemistry, 2002

May 2013
University of Arkansas

ABSTRACT

Synthesis of InP/ZnS core/shell nanocrystals and TiO_2 nanotubes and the optimization study to couple them together were explored for quantum dot sensitized solar cells. Its intrinsic nontoxicity makes the direct band gap InP/ZnS core/shell be one of the most promising semiconductor nanocrystals for optoelectric applications, with the advantage of tuning the optical absorption range in the desired solar spectrum region. Highly luminescent and monodisperse InP/ZnS nanocrystals were synthesized in a non-coordinating solvent. By varying the synthesis scheme, different size InP/ZnS nanocrystals with emission peaks ranging from 520 nm to 620 nm were grown. For the purpose of ensuring air stability, a ZnS shell was grown. The ZnS shell improves the chemical stability in terms of oxidation prevention. Transmission electron microscopy (TEM) image shows that the nanocrystals are highly crystalline and monodisperse.

Free-standing TiO_2 nanotubes were produced by an anodization method using ammonium fluoride. The free-standing nanotubes were formed under the condition that the chemical dissolution speed associated with fluoride concentration was faster than the speed of Ti oxidation. Highly ordered free-standing anatase form TiO_2 nanotubes, which are transformed by annealing at the optimized temperature, are expected to be ideal for coupling with the prepared InP/ZnS nanocrystals.

Electrophoretic deposition was carried out to couple the InP/ZnS nanocrystals with the TiO_2 nanotubes. Under the adjusted applied voltage condition, the current during the electrophoretic deposition decreased continuously with time. The amount of the deposited nanocrystals was estimated by calculation and the evenly deposited nanocrystals on the TiO_2 nanotubes were observed by TEM.

This thesis is approved for recommendation
to the Graduate Council.

Thesis Director:

_____
Dr. Omar Manasreh

Thesis Committee:

_____
Dr. Simon Ang

_____
Dr. Scott Smith

THESIS DUPLICATION RELEASE

I hereby authorize the University of Arkansas Libraries to duplicate this thesis when needed for research and/or scholarship.

Agreed _____

Seungyong Lee

Refused _____

Seungyong Lee

ACKNOWLEDGEMENTS

First of all I would like to express my appreciation to my parents and all my family members for their love and support.

I would like to give my deep gratitude to my graduate advisor and thesis director, Dr. Omar Manasreh for providing me an opportunity to research this project with great supervision.

I am thankful to Dr. Simon Ang and Dr. Scott Smith for being in my thesis committee and helping me to complete this project.

I wish to thank my group members, Dr. Scott Little, Dr. Mahmood Khan, Rick Eyi, Yahia Makableh, Ramesh Vasan, Jony Chandra Sarker, Ahmad Nusir, and Dr. Jiang Wu for their support and help in completing this project.

"If we knew what it was we are doing, it would not be called research." - Albert Einstein

This work was partially supported by the Air Force Office of Scientific Research (Grant FA9550-10-1-0136), the NSF-EPSCoR program (Grant EPS-1003970), and NASA-EPSCoR program (Grant 242026-1BBX11AQ36A).

TABLE OF CONTENTS

LIST OF FIGURES

LIST OF ACRONYMS

AM	Air mass
CVD	Chemical vapor deposition
DDT	Dodecanthiol
DSSC	Dye sensitized solar cell
EDX	Energy dispersive X-ray
EPD	Electrophoretic deposition
FF	Fill factor
FTO	Fluorine doped tin oxide
$In(Ac)_3$	Indium acetate
$In(Mt)_3$	Indium myristate
ODE	Octadecene
$P(TMS)_3$	Tris(trimethylsilyl)-phosphine
PVD	Physical vapor deposition
QDSSC	Quantum dot sensitized solar cell
SEM	Scanning electron microscopy
TCO	Transparent conductive oxide
TEM	Transmission electron microscopy
UV-Vis	Ultraviolet-visible spectroscopy
XRD	X-ray diffraction

1. OVERVIEW

1.1 Introduction

Demand for renewable energies with a growing world population has brought interest to solar energy which can be a clear solution to an energy scarcity. Since we sought alternative resources from the origin of energy, silicon based crystalline or amorphous solid-state junction devices have dominated the solar cell industry [1-3]. However, in an effort to lower the cost and improve the manufacturability, different semiconductor technologies for photovoltaics have been intensively developed [1]. Among many promising solar cell technologies, the solar cells that are based on the sensitization of inorganic oxide films by dyes or quantum dots have been drawing an increasing awareness [2]. These solar cells have the possible advantages of low fabrication cost along with high energy conversion efficiency, a variety of applications satisfying the customer's demand, and high availability with ultrathin and flexible characteristics [1]. For these fascinating solar cells, two novel semiconductor materials are required as key components. One of them is a nanostructured semiconductor oxide film that provides microscopic surface area, orders of magnitude larger than their geometric area. The other is a narrow bandgap semiconductor, namely a sensitizer, which mainly absorbs incident photon and transports excited electrons to the semiconductor oxide electrode [2]. Coupling these two semiconductors is also a challenge to fabricate high performance solar cells. A hole conductor material is placed in contact with a sensitizer to restore it back to the original state by electron donation [4].

TiO_2 is very promising semiconductor oxide since it is photostable, cheap, non-toxic, and easily applicable [5-6]. It is capable of efficiently harvesting light as well as being a prominent anode electrode in solar cells. The most widely used photoelectrode in dye sensitized solar cells

(DSSCs) is porous TiO_2 films made from TiO_2 nanocrystalline particles [7]. However, they are considered inferior to TiO_2 nanotube structure with respect to more charge recombination and low mobility [7]. For this reason, TiO_2 nanotubular structure has been intensively researched for high efficiency solar cells.

Pure TiO_2 with relatively wide band gap is photoactive only in the ultraviolet region. Thus solar light cannot be fully utilized. Therefore, TiO_2 needs to be coupled with a sensitizer which is able to extend the absorption range to the visible region and even to the infrared range for high efficiency [7]. Since the conceptual DSSC was first reported in 1991, considerable efforts have been devoted to designing new dyes for visible light harvesting over the entire spectrum [8,9]. The most efficient DSSC so far uses Ru-based dyes [10,11]. As a sensitizer, organic dyes are sufficient in extending the range of light absorption but their short life time and instability for practical applications have been moving an interest towards quantum dots with a broad spectrum as a replacement for organic dyes [12]. Some low band gap semiconductor nanocrystals such as CdS or CdSe quantum dots can significantly improve the solar cell stability [12]. The property of being able to alter the band gap makes a great contribution to increasing the efficiency as well. CdSe and CdS quantum dots with excellent photostability, and quantum yield have limited applications owing to their intrinsic toxicity [13]. Therefore, it is believed that InP is the most desirable alternative with nontoxicity [13]. However, poor emission efficiency, difficulty in controlling size distribution and chemical instability are the existing problems, which should be improved in order to be used as a sensitizer [13].

This work presents optimized TiO_2 nanotubes and InP/ZnS core/shell nanocrystals for quantum dot sensitized photovoltaic solar cells. In general, TiO_2 nanotubular form is expected to enhance charge transfer and reduce interfacial charge recombination, which is due to shorter

travel distance and highly ordered contact architecture [12]. For the growth of TiO_2 nanotubes, an anodic oxidation method is used to obtain uniform and orderly arranged nanotubes with controllable pore size and length. The TiO_2 nanotubes are produced by anodization using ammonium fluoride. For its application to solar cells, highly ordered nanotubes with minimal defects such as bundling, sealing, cracks are required to enhance the mobility of electrons. Crystalline form of TiO_2 can be obtained by annealing after amorphous TiO_2 is produced. Optimized crystallinity can reduce the gap of grain boundaries and eliminate the charge recombination sites, which is very important for the fabrication of high performance photovoltaic devices [12]. As a sensitizer, highly luminescent InP/ZnS core/shell nanocrystals are synthesized under a thorough degassing process. By controlling the synthesis scheme and reaction parameters, different size InP/ZnS nanocrystals were grown. In order to ensure air stability, ZnS shell was grown on the top of the InP core. This ZnS shell improves the chemical stability in terms of oxidation prevention [13]. For the fabrication of quantum dot sensitized solar cells, electrophoretic deposition (EPD) method is applied to couple the InP/ZnS nanocrystals with the TiO_2 nanotubes. For the EPD process under constant voltage conditions, current decreases continuously with time. This is the evidence that the deposition is progressed with an increase in electric resistance.

1.2 Semiconductor Nanocrystals

A semiconductor has a band gap, which is the energy difference between the conduction and the valence band, as shown in Figure 1.1 (a) and (b). Upon absorption of light, electrons are excited from the valence band to the conduction band. When an electron jumps to the conduction band the excited electron leaves behind a localized positively charged hole in the valence band.

The negative charge electron in conduction band is attracted to this localized hole by the electrostatic Coulomb force [14]. The bound state of an electron and hole is defined as an exciton.

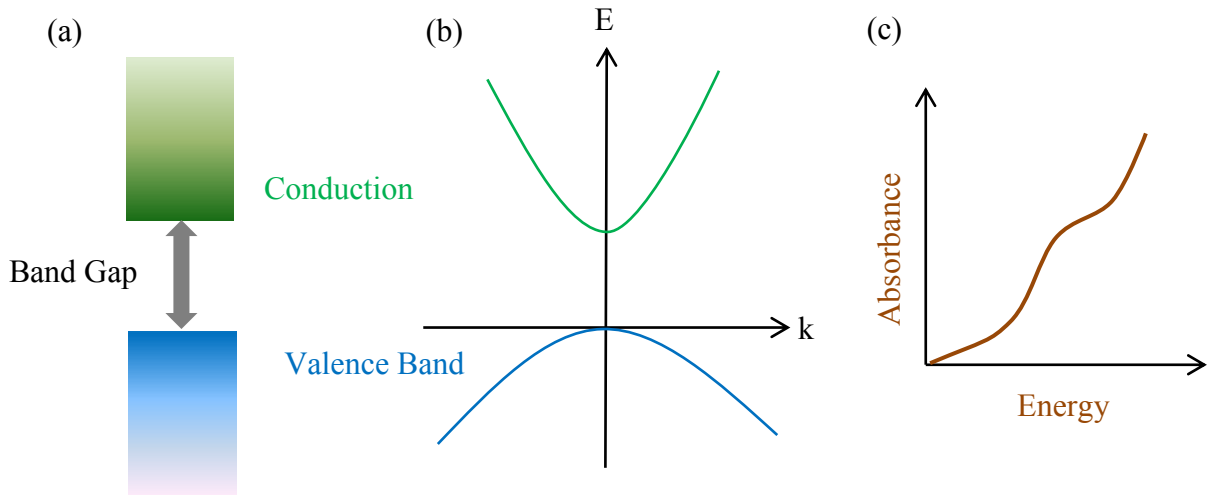

Figure 1.1 Representations of the energy band diagram of a semiconductor material and its typical absorbance spectroscopy: (a) The continuous levels of the conduction and valence bands and the band gap are shown in real space. (b) The same conduction and valence bands are plotted as a function of wavevector (k) in reciprocal space. (c) The standard absorbance for a direct band bulk semiconductor is shown.

In analogy with a hydrogen atom, the lowest energy set of states is composed of closely bound electron-hole pair configurations [15]. For most semiconductor nanocrystals, this binding energy is relatively small compared to the band gap.

In an effort to incorporate molecular-like behavior in standard semiconductor materials, nanoscale semiconductor structures have been investigated over the past several decades. Interest in new materials with specific optical properties has driven the development of quantum wells, quantum wires, and quantum dots [14]. The effects of quantum confinement take place when the

quantum well thickness becomes comparable with the de Broglie wavelength of carriers [14]. Quantum dots have three confinement directions and zero degree of freedom directions. The most striking phenomenon of quantum dots is a change in optical properties as a function of nanocrystal size. Continuous electronic bands are altered to discrete or quantized electronic levels [14]. As a result, the continuous optical transition between bands becomes discrete and nanocrystals which have the discrete energy levels have a size dependent property [14].

Semiconductor nanocrystals are used as a photosensitizer which plays a key role in extending the absorption range to the visible region and even to the infrared range. Since the conceptual dye-sensitized solar cell (DSSC) was first reported in 1991 [1], numerous efforts have been devoted to designing new dyes for entire visible light harvesting and solar cell efficiency has been reached up to 11% as the highest record [16]. Although organic dyes are ideal in absorbing light, attempts to lower the cost and improve the stability for practical applications are in the intensive research. Some low band gap semiconductor nanocrystals such as CdS or CdSe quantum dots can significantly improve the stability of the solar cells. These quantum dots, however, have limited applications owing to their intrinsic toxicity [13]. Therefore, InP quantum dots are believed to be the most desirable alternative because it is intrinsically nontoxic.

1.3 Titanium Dioxide

Oxide semiconductor materials, especially TiO_2, are chemically stable under the visible and UV irradiations. In addition, they are nontoxic and relatively inexpensive. Nanoparticulate TiO_2 has been produced conventionally by chemical synthesis such as a sol-gel process [17]. A particulate TiO_2 layer, generally 5 to 15 μm, consists of interconnected nanoparticles of the size ranging from 5 nm to 30 nm [17]. When this nanoporous structure with high surface area is used

in dye sensitized solar cells, the amount of dye material deposited on the TiO_2 surface is drastically increased. This results in an increase of light harvesting efficiency. The most widely used photoelectrode in DSSCs is porous TiO_2 films made from nanocrystalline TiO_2 particles. In general, the dynamic competition between the electron flow in TiO_2 and the interfacial charge recombination is a main factor to limit the solar cell efficiency [12]. In the nanoparticle structures, numerous trapping sites, long travel distance, and disordered contact areas result in drawbacks of more charge recombination and enhanced scattering of free electrons with the reduced mobility [12]. By creating direct pathways for accelerating the charge transfer between interfaces, a nanotubular TiO_2 structure is expected to enhance the electron transporting and the charge separation efficiency [4]. A highly ordered, vertically oriented tubular structure increases electron mobility along the tube axis perpendicular to the substrate, reducing interface recombination. Enhanced internal and external surface area is available for more sensitizer loading, particularly in TiO_2 nanotube-based electrodes [12].

In 1999, Zwilling and co-workers first reported a TiO_2 porous film grown on a titanium sheet by anodic oxidation at a low voltage [18]. Grimes group in 2001, when they initiated the nanotubes formed in an HF aqueous electrolyte up to 0.5 μm in length [19]. An anodic oxidation method is more simple and convenient than a hydrothermal or template method for uniform and orderly arranged nanotubes perpendicular to the substrate with controllable pore size and length [12]. The aqueous solution containing hydrofluoric acid limits further growth of TiO_2 over several μm in length, which results from a high rate of chemical dissolution [12]. In order to grow nanotubes long enough to have large surface area with high absorption efficiency, a neutral fluoride solution with a low acidity environment was introduced, leading to a tube length of up to 4 μm [20]. When it comes to preparation of TiO_2 nanotubes, fluoride ions, chlorine or bromide-

based electrolytes are suitable but most of the TiO_2 nanotubes are obtained in the solutions containing fluorinated electrolytes [12].

In most studies, the morphology of TiO_2 nanotubes is not uniform enough and there are many defects such as bundling, sealing, over-etching or cracks, affecting on their photoelectric properties [12]. The bundling brings a greater chance of recombination in TiO_2 nanotube solar cells as well as it leads to a large number of cracks on the top surface in TiO_2/polymer solar cells, which is not preferable for building ordered p-n heterojunction structures [12]. The over etching can also lead to aggregation of dyes and poor contact with a counter electrode [12]. Therefore, it is important not to have these defects in TiO_2 nanotubes.

The performance of solar cells highly depends on crystalline forms of TiO_2 [12]. Annealing which influences the crystalline form cannot only improve the crystallinity but also reduce the gap of the grain boundaries [12]. Optimized crystallinity of TiO_2 nanotubes is very important for the fabrication of high performance photovoltaic devices.

1.4 Dye/Quantum Dot Sensitized Solar Cells

The relatively wide band gap of TiO_2 needs to combine with a solar absorbing material in order to extend the absorption spectrum to the visible region. Organic dyes and narrow band gap nanocrystalline quantum dots are used as such sensitizers [12].

The first dye sensitized solar cell (DSSC) included the organic dye, nanocrystalline TiO_2 porous films as the photoanode and redox pair reactions of I_3^-/I_2 couples to complete the circuit [1]. Since then, considerable efforts has been focused on new dyes for visible light harvesting over the entire spectrum. So far the most efficient DSSCs use Ru-based dyes with over 11% efficiency [12]. Figure 1.2 shows the ruthenium complex dye chemisorbed on TiO_2 surface and

photocurrent spectra with different dyes. Developing new dyes with high molar absorption coefficients and a wider coverage of the solar spectrum can be realized by a synthetic chemical protocol. On the other hand, the surface modification of TiO_2 such as carboxyl functionalized Si nanoparticles and graphene incorporation is also promising due to the effect of enhanced charge transfer [21].

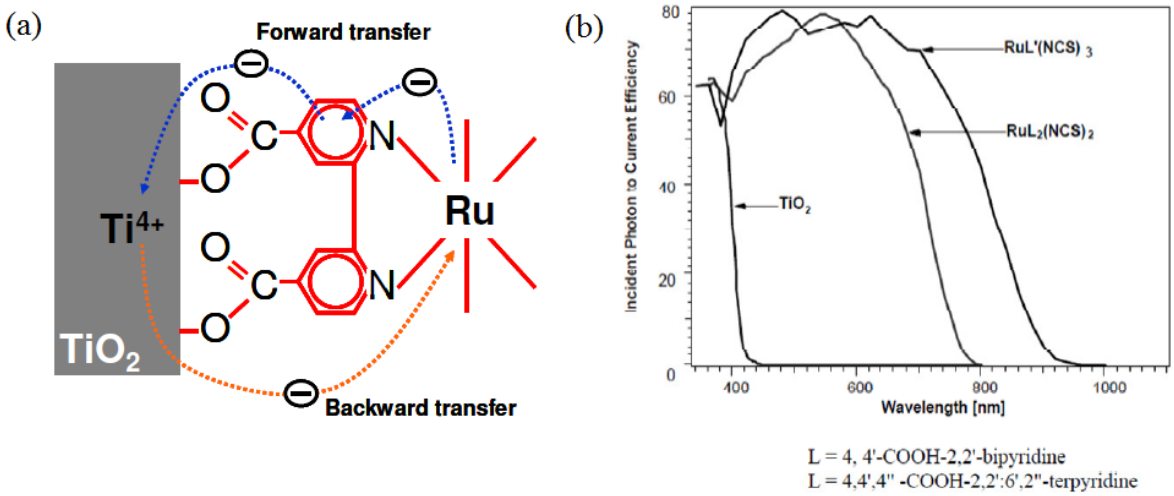

Figure 1.2 (a) Chemical structure of ruthenium complex dye chemisorbed on titanium oxide surface [22] (b) Photocurrent spectra of the N3 (ligand L), the black dye (ligand L′) as sensitizer and bare TiO_2 films for comparison [23].

The most attractive points of TiO_2 nanotubes are the capability to shorten the electron transport distance and reduce recombination. Figure 1.3 shows TiO_2 nanoparticles and nanotubes and their electron path respectively. Schmuki and co-workers demonstrated the first anodized TiO_2 nanotube-based DSSCs using an organic dye, which opened a new page for TiO_2 nanotube-based DSSCs [24]. In order to improve the efficiency, TiO_2 nanotubes of different lengths have been studied, consequently reaching to 2-3%, which is still far behind the conventional TiO_2

nanocrystalline film-based DSSCs [12]. In order to expand applications of TiO_2 nanotubes, a highly ordered structure is needed and optimized coupling with dyes is also required.

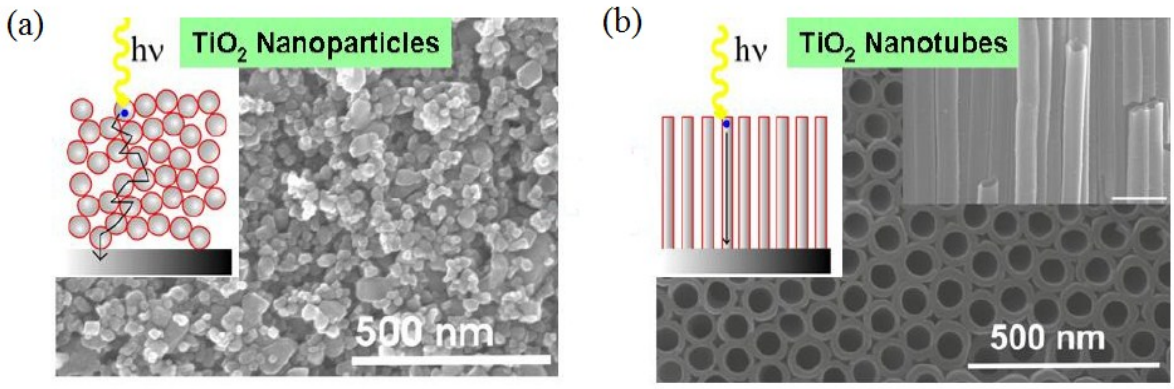

Figure 1.3 (a) SEM image and the electron path of TiO_2 nanoparticles (b) SEM image and the electron path of TiO_2 nanotubes [25].

Although organic dyes are enough to be a good sensitizer, the high cost and instability for practical applications request their alternatives [12]. Low band gap quantum dots can fulfill the requirements with the property to alter the band gap for a wider spectrum response [12]. The quantum dots adsorbed onto TiO_2 materials have excited electrons on the conduction band by photons. In order to transport the electrons to the TiO_2, the conduction band energy level of quantum dots should be higher than that of the TiO_2 [12]. In quantum dot solar cells, photo-degradation of quantum dots put a limit to the usage life time. By coating a thin film of amorphous TiO_2 around the quantum dot sensitized electrode, solar cell efficiency as well as photostability can be improved, which results from blocking charge recombination paths [12]. In addition, a photo-corrosion problem can be solved by growing ZnS shell around a quantum dot core [26].

Conductive polymers have received extensive attention because TiO_2 nanotubes or fullerene derivatives in combination with them provide a great opportunity to make ordered heterojunction solar cells [27]. A key issue of these hybrid solar cells is interfacial incompatibility, which causes phase separation and ultimately constrains exciton separation [12]. In order to improve the bond strength between an inorganic phase (TiO_2) and an organic one (conductive polymer) a self-assembly strategy was introduced [28]. Conductive polymer can be anchored effectively onto the inorganic phase by carboxyl groups or catalyst-transfer polycondensation [28]. How to effectively bond or initiate surface polymerization would determine potential applications in hybrid solar cells.

The most widely used electrolyte in DSSCs contains I^-/I_3^- redox ions, which mediate electrons between the sensitizers and the counter electrode. Typical organic solvents used for DSSCs are nitrile solvents which have relative low viscosity. Viscosity of solvents directly affects ionic conductivity in an electrolyte as well as the solar cell performance [29]. Although an iodide electrolyte is compatible with the ruthenium-based dyes in the DSSCs, it degrades nanocrystals in the quantum dot sensitized solar cells (QDSSCs), lowering the device performance. S^{2-}/Sn^{2-} redox ions that provide stability are expected to be compatible with nanocrystal sensitizer-based devices [30, 31]. There are limitations in nanocrystal materials that can be used with a sulfide electrolyte as well. For instance, NaS stabilizes CdSe and CdS nanocrystals but degrades CdTe nanocrystals [32]. The reaction that occurs in the CdTe system results in the formation of a sulfide layer, affecting the performance of the device [32]. Faster emission decay in the presence of a NaS electrolyte is observed as compared to emission decay in air [32].

In the system in which an electrolyte is employed, a counter electrode has a significant effect on the device performance. Platinum or graphite is a widely used counter electrode, which ensures to maintain the device efficiency. Although platinum is commonly used for an electrode, it has been shown to have much higher series resistance with polysulfide electrolytes than with iodide electrolytes [33]. It has been suggested that series resistance is increased due to the attachment of a polysulfide electrolyte to a platinum electrode [33]. The continued use of platinum as an electrode is considered as a critical factor to lower the device performance compared to their counterparts. A replacement of platinum would contribute to reducing the cost of the device materials as well as increase the efficiency of nanocrystal-based solar cells.

2. THEORY

2.1 Preparation of Nanostructures of Different Shapes

2.1.1 Nucleation and Particle Growth

Chemical growth of bulk or nanosize materials inevitably goes through the process of precipitation of a solid phase from solution. In order to obtain nanoparticles with desired size and shape, a good understanding of the process and the parameters controlling the precipitation is very important. For a particular solvent, there is a certain solubility for a solute. When any excess solute is added to the solution, it results in precipitation and formation of nanocrystals. In order to initiate nanoparticle formation, for nucleation to occur, a solute is dissolved at higher temperature and then cooled to low temperature to make the solution supersaturated [34]. Another way is to add needed reactants to obtain a supersaturated solution during the reaction [34]. This nucleation step and particle growth stages following the nucleation are basic components of a precipitation process [35].

Homogeneous nucleation, heterogeneous nucleation, and secondary nucleation are typical methods for nucleation processes. Homogeneous nucleation results from combining solute molecules to produce nuclei in the absence of a solid interface. The driving force of the thermodynamics gives rise to homogeneous nucleation because the supersaturated solution is not stable in energy. The overall free energy change, ΔG, is the sum of the free energy from the formation of a new volume and the free energy from the new surface created. For spherical particles [14]:

$$\Delta G = -\frac{4}{V}\pi r^3 k_B T In(S) + 4\pi r^2 \gamma \qquad (2.1)$$

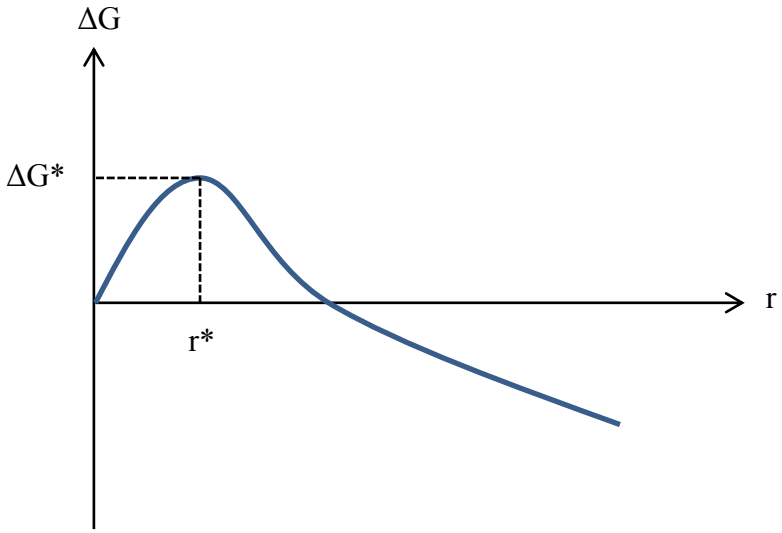

Figure 2.1 Illustration of the overall free energy change, ΔG as a function of the growth particle size r [14].

Where V is the molecular volume of the precipitated species, r is the radius of the nuclei, k_B is the Boltzmann constant, S is the saturation ratio, and γ is the surface free energy per unit surface area. When S > 1, ΔG has a positive maximum at a critical size, r*. This maximum free energy corresponds to the activation energy for nucleation. Nuclei larger than the critical size will further decrease their free energy for growth. The stable nuclei with decreased free energy grow to form particles. The critical nuclei size r* can be obtained by setting dΔG / dr = 0 [14]:

$$r^* = \frac{2V\gamma}{3k_B TIn(S)} \tag{2.2}$$

For a given value of S, all particles with r > r* will grow and all particles with r < r* will dissolve. From the above equation, it follows that as the saturation ratio S becomes high, the critical nuclei size r* becomes small [14]. After the nuclei are formed from the solution, they go

into growth stages via molecular addition, which relives the supersaturated step. When the concentration of a solute drops below the critical level, the nucleation stops and the particle growth continues by molecular addition until the equilibrium concentration of the precipitated species is reached. A short nucleation period that generates all of the particles facilitates uniformity of the particle size distribution. The nucleation period is followed by a self-sharpening growth process. At this stage, the smaller particles grow more rapidly than the larger ones due to the fact that the free energy driving force is larger for smaller particles than for larger ones when the particles are slightly larger than the critical size. Particle size distribution can be controlled at this stage and nearly monodisperse size distribution can be obtained by either stopping both nucleation and growth quickly or by supplying reactant source to keep a saturated condition during the reaction. When the reactants are depleted owing to particle growth, Ostwald ripening occurs, where small particles dissolve and large particles continue to grow due to the deposition of the dissolved small particles. Ostwald ripening is a phenomenon which describes the change of an inhomogeneous structure. This spontaneous process occurs thermodynamically because larger particles are more energetically stable than small particles. This stems from the fact that the surface atoms, which are surrounded by fewer neighbor atoms than the atoms inside the particle, are energetically less stable. Over time, the molecules on the surface of small particles tend to detach from the particles and diffuse into the solution and then redeposit on the surface of larger particles [36]. According to the equation above, as the saturation ratio (S) decreases the corresponding critical size (r*) increases. Therefore any particles smaller than this new critical size will dissolve. If the reaction is quickly stopped at this stage, a broad size distribution will be obtained. Once the reaction goes into this ripening stage, the reaction needs to be extended to long enough time to completely deplete the supersaturation and the smaller

nuclei in order to obtain monodisperse particles. If there is no continuous supply of the reactants, the decrease of saturation ratio causes the increase of the critical nuclei size. In addition to the growth by molecular addition where dissolved molecules detached from small particles redeposit on large particles, particles can grow by aggregation with other particles, which is called secondary growth. The rate of particle growth by the secondary growth is much larger than that by molecular addition [14].

2.1.2 Preparation Methods

The sol-gel method based on inorganic polymerization reactions includes four steps: hydrolysis, polycondensation, drying, and thermal decomposition. Precursors of metal or nonmetal alkoxides hydrolyze with water or alcohols through the hydrolysis process [14].

$$M(OR)_x + mH_2O \rightarrow M(OR)_{x-m}(OH)_m + mROH$$

Where if m is up to x, total hydrolysis occurs, followed by either a water condensation [14]

$$2M(OR)_{x-m}(OH)_m \rightarrow (OH)_{m-1}(OR)_{x-m}{-}M{-}O{-}M(OR)_{x-m}(OH)_{m-1} + H_2O$$

or an alcohol condensation [14].

$$2M(OR)_{x-m}(OH)_m \rightarrow (OH)_{m-1}(OR)_{x-m}{-}M{-}O{-}M(OR)_{x-m-1} + ROH$$

The total reaction can be expressed as [14].

$$M(OR)_x + x/2\ H_2O \rightarrow MO_{x/2} + xHOR$$

After the solution has been condensed to a gel, the final product is obtained by removing the solvent. The size of particles can be controlled by adjusting solution composition, pH, and temperature [14].

Chemical precipitation can be achieved by controlling of the kinetics of the precipitation. The kinetics of nucleation and particle growth in homogeneous solutions can be adjusted by

anions and cations generated from organic molecules. The concentration of the reactants and ions and pH are the essential factors, which determine the precipitation process and influence the particle size [14].

Hydrothermal synthesis is a method to exploit the solubility of inorganic material in water at elevated temperatures and pressure and subsequent crystallization of the dissolved material from the fluid. Water at elevated temperatures has an effect on the precursor material transformation due to the increased vapor pressure. High temperatures also change the solubility and reactivity of the reactants, which can produce different high quality nanoparticles and nanotubes. In hydrothermal synthesis, water pressure, temperature, and reaction time can be controlled to maintain a high simultaneous nucleation rate and narrow size distribution [14].

Pyrolysis is a chemical process in which chemical precursors decompose at elevated temperatures without the participation of oxygen. Upon completion, powder form of the desired substance with wide size distribution is obtained. In order to produce a uniform nanosize material, a change of the reaction rate or decomposition of the precursor in the inert solvent is performed [14].

In chemical vapor deposition (CVD), the vaporized precursors are deposited onto the substance held at an elevated temperature. These absorbed molecules onto the substance either thermally decompose or react with other gases to form crystals. The precursors can be deposited through a boundary layer by diffusion or chemical reaction on the growth surface. Gas-phase reaction byproducts are removed from the growth surface [14].

Physical vapor deposition (PVD) involves condensation from the vapor phase. Three main steps in PVD process are the generation of a vapor phase by evaporation or sublimation of

the material, transporting the material from the source to the substrate, and formation of the particle by nucleation and growth [14] .

2.2 Optical and Electrical Properties of Nanoparticles

2.2.1 Discrete Electronic Structure

Quantum confinement is a widely used terminology in the study of nanocrystals since in the nanometer regime the electronic structure is altered from continuous electronic bands to quantized energy levels. The continuous optical transitions between the electronic bands become discrete and the optical properties are dependent on the size of materials [14]. The size dependence of the nanocrystal absorption and emission spectra is determined by the modified energy levels of three-dimensionally confined quasiparticles [37]. In a spherical nanocrystal surrounded by an infinite potential barrier, the quantized energy of the electron is given by the following parabolic approximation [37]:

$$E_{l,n}^{e} = \frac{\hbar^2 \phi_{l,n}^2}{2m_e^* a^2} \quad , \quad E_{l,n}^{h} = \frac{\hbar^2 \phi_{l,n}^2}{2m_h^* a^2} \tag{2.3}$$

Where l is angular momentum quantum number, $m_{e,}^*$ m_h^* are electron and hole effective mass respectively, $\phi_{l,n}$ is the n th root of the spherical Bessel function of order, and a is the crystal radius. As nanocrystal size decreases, the total energy of optical transitions between the quantized electron levels and hole levels increases. In addition, there exists the Coulomb interaction between the optically created electron and hole pair. The Coulomb energy of the electron and hole interaction is on the order of $e^2/\epsilon_r a$, where ϵ_r is the dielectric constant of the semiconductor. In small nanocrystals, the Coulomb energy is less significant because the

quantization energy increases with decreasing size as $1/a^2$ while the Coulomb energy grows only as $1/a$. Therefore, small correction to the quantization energies is required and transition energies are reduced by only a relatively small amount. On the other hand, in large nanocrystals, the Coulomb interaction should be necessarily taken into account with the quantization energies of the electrons and holes. The optical properties of nanocrystals are dependent on the ratio of the nanocrystal radius, a, to the Bohr radius of the bulk exciton, $a_B = \hbar^2\epsilon_r/\mu e^2$, where μ is the exciton-reduced mass and ϵ_r is the dielectric constant of the semiconductor [37]. With regard to the relationship of the radius of the crystal to the Bohr radius of the bulk exciton, the quantum confinement effect can be divided into three regimes: weak confinement when $a \gg a_B$, intermediate confinement when $a_e > a > a_h$, in which $a_e = \hbar^2\epsilon_r/m_e^* e^2$ and $a_h = \hbar^2\epsilon_r/m_h^* e^2$, and strong confinement when $a \ll a_B$, respectively. The weak confinement regime can be realized in large crystals. In this regime, the optical spectra of nanocrystals are determined by the quantum confinement of the exciton center of mass because the binding energy of the exciton, E_{ex}, is larger than the quantization energy of both the electrons and holes [37]. The intermediate confinement regime corresponds to $a_e > a > a_h$ and electrons and holes have different values of effective masses. In this regime, the electron moves much faster than the hole because the hole is confined in the average potential of the electron and is localized at the center of the nanocrystal [37]. The nanocrystal central area where the hole is moving is much smaller than the nanocrystal radius and the size dependence of the exciton ground state can then be described as the behavior of a donor localized at the nanocrystal center. The excitation spectrum of such a donor-like exciton can be described in terms of oscillation of the hole about the crystal center. Strong confinement regime realized in the small nanocrystals has small electron-hole Coulomb interaction and the optical spectra can be considered as the spectra of transitions between

electron and hole quantum size levels. Interband transitions are allowed only between quantum size levels with the same quantum numbers. The transition energy can be expressed by [37]:

$$\hbar\omega_v = E_g + E_v^h(a) + E_v^e(a) - 1.8\frac{e^2}{4\pi\epsilon_r\epsilon_0 a} \tag{2.4}$$

Where the Coulomb correction is calculated in first order perturbation theory [38].

2.2.2 Quantum Dots

A quantum dot is characterized by having three confinement directions and zero degree of freedom directions. Because of the lack of dispersion curves the wavevector selection rules are absent. The density of states thus contains a series of delta functions centered on the confined energy levels. The energy levels are entirely discrete and are given by:

$$E_{n_x,n_y,n_z} = \frac{\hbar^2\pi^2}{2m^*}\left(\frac{n_x^2}{L_x^2} + \frac{n_y^2}{L_y^2} + \frac{n_Z^2}{L_Z^2}\right) \tag{2.5}$$

Where L_x, L_y, and L_z are the dimensions of the quantum dot and n_x, n_y, and n_z are positive integers. In a semiconductor the energy bands for free electrons and holes are separated by an energy gap and the states are continuous. In a quantum dot the charges are confined.

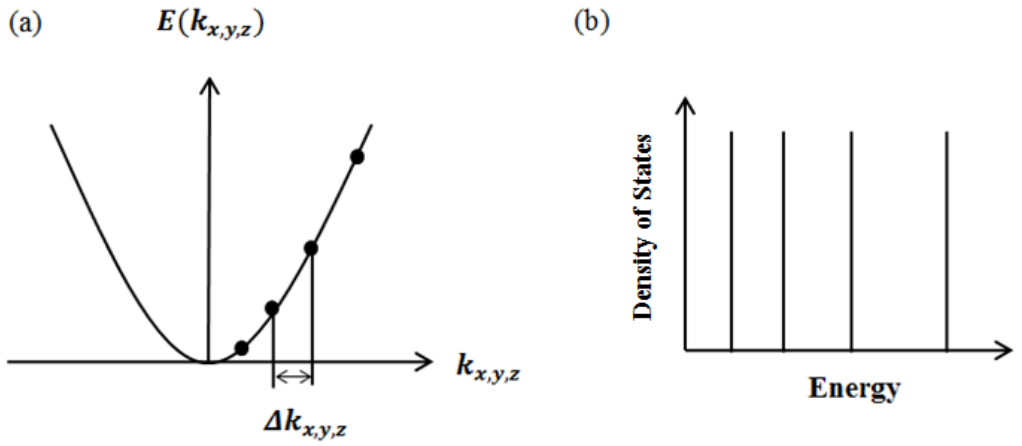

Figure 2.2 (a) The electron energy E(k) for electrons in a zero-dimensional bulk solid shows the only allowed discrete energy levels. (b) The zero-dimensional density of states.

This can be described as a charge carrier confined in an infinite potential well of width d. The width d of the potential well corresponds to the diameter of the quantum dot shown in Figure 2.3.

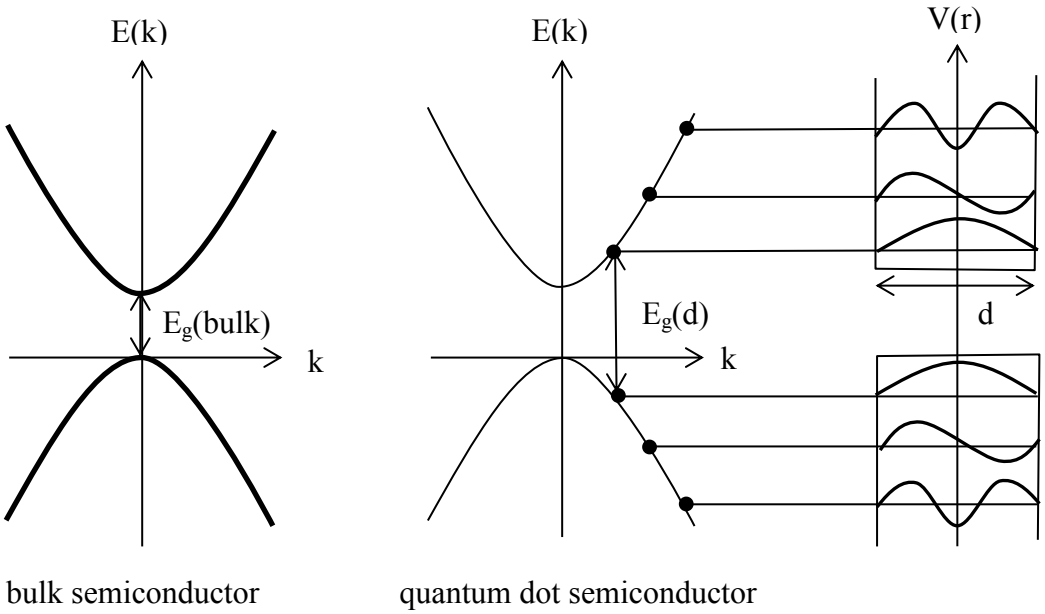

Figure 2.3 Energy levels of a bulk semiconductor and a quantum dot.

This quantum confinement arises as a result of changes in the density of states and can be explained by the relation between position and momentum in free and confined particles. For a free particle both the energy and the momentum are precisely defined, while the positions are not defined well. For a localized particle, the momentum is no longer well defined because the uncertainty in position decreases. The discrete energy of the particle may then be represented as superpositions of bulk momentum states. A single, intense transition in a quantum dot occurs since a series of nearby transitions occurring at different energies in the bulk is compressed by quantum confinement. In a quantum dot, the energy band gap increases as the particle size decreases because the quantum confinement shifts the energy levels of the conduction band and valence band. The band gap E_g^* (eV) can be obtained using the effective mass model for spherical particles with a Coulomb interaction term [15]:

$$E_g^* = E_g^{bulk} + \frac{\hbar^2 \pi^2}{2r^2}\left(\frac{1}{m_e^*} + \frac{1}{m_h^*}\right) - \frac{1.8\, e^2}{4\pi \epsilon_r \epsilon_0 r} \tag{2.6}$$

Where r is the particle radius, m_e^* is the effective mass of the electrons, $m_h^*$is the effective mass of the holes, ϵ_r is the relative permittivity, ϵ_0 is the permittivity of free space, and e is the charge of the electron. The band structure of semiconductors is more complicated than the parabolic effective mass approximation. While in many cases the conduction band is well approximated by the effective mass model, the valence band is not well approached by the model. Spin-orbit coupling, crystal field splitting, and intraband coupling give rise to a more precise band structure to the valence band. Due to spin-orbit coupling the valence band is split into two bands, split-off band and light and heavy hole bands. In some cases due to the crystal field the light hole and heavy hole are further split.

2.3 TiO_2 Nanotubes

2.3.1 Formation of Anodic TiO_2 Nanotube Arrays

In the first work by Zwilling *et al*. [18] not ordered TiO_2 nanotubes with a few hundred nanometers in length could be obtained. These structures turned out to have a tubular form and have been optimized in the past years [19]. In principle, highly ordered and self-organized TiO_2 nanotube arrays can be obtained by anodization of titanium in electrolytes with fluoride ions. The chemical reactions driven by electric field specifically for anodization of titanium are described as [39]:

At Ti/Ti oxide interface:

$$Ti \leftrightarrow Ti^{2+} + 2e^{-} \tag{2.7}$$

At Ti oxide/electrolyte interface:

$$2H_2O \leftrightarrow 2O^{2-} + 4H^{+} \tag{2.8}$$

At both interfaces:

$$Ti^{2+} + 2O^{2-} \leftrightarrow TiO_2 + 2e^{-} \tag{2.9}$$

As a result, oxygen ions react with Ti to from oxide. The as-formed TiO_2 layer can be protective and prohibit further oxidation because the layer is passive with limited ionic conductivity. At anode under a high applied voltage, Ti^0 is oxidized to Ti^{4+} or Ti^{2+} at the metal-oxide interface and the cations migrate outwards and O^{2-} ions are incorporated in the layer and migrate towards the metal-oxide interface. A compact titanium oxide layer is formed by these

reactions. Depending on the transfer properties of anions and cations in the oxide lattice, the TiO_2 layer may grow at the outer or inner of the oxide interface. When the electrolyte contains fluoride ions, dissociation of titanium and titanium oxide occurs simultaneously by a chemical etching process, which is described as [39]:

$$TiO_2 + 6F^- + 4H^+ \rightleftharpoons TiF_6^{2-} + 2H_2O \quad (2.10)$$

During the anodization process, the oxidation and field-driven ion diffusion occur simultaneously. The formation of highly-ordered TiO_2 nanotube arrays results from the competition of these two processes, field-assisted oxidation of Ti metal to form titanium oxide and chemical dissolution of Ti and TiO_2 due to the chemical etching by fluoride ions. The final chemical dissolution of TiO_2 in the electrolyte containing fluoride ions plays a pivotal role in the formation of the highly ordered TiO_2 nanotube arrays. The initial stages of the anodization process with fluoride ions were extensively investigated and reported that the field-assisted dissolution dominates the chemical dissolution because of the relatively large electric field across the titanium oxide layer [40]. Then small pits form due to the localized dissolution of the titanium oxide, serving as starting pore centers. These pits are subsequently grown up to bigger pores and cover uniformly over the surface. The understanding of the formation of the anodic TiO_2 nanotube arrays stems from the mechanism of the formation of alumina pores developed by Parkhutik and Shershulskii [41], as shown in Figure 2.4. At the beginning of the anodization process, a compact and uniform titanium oxide layer is formed on the surface, as shown in Figure 2.4 (a). The distribution of electric field in the oxide layer is strongly associated with surface morphological fluctuations, which determines the formation of the pore structures.

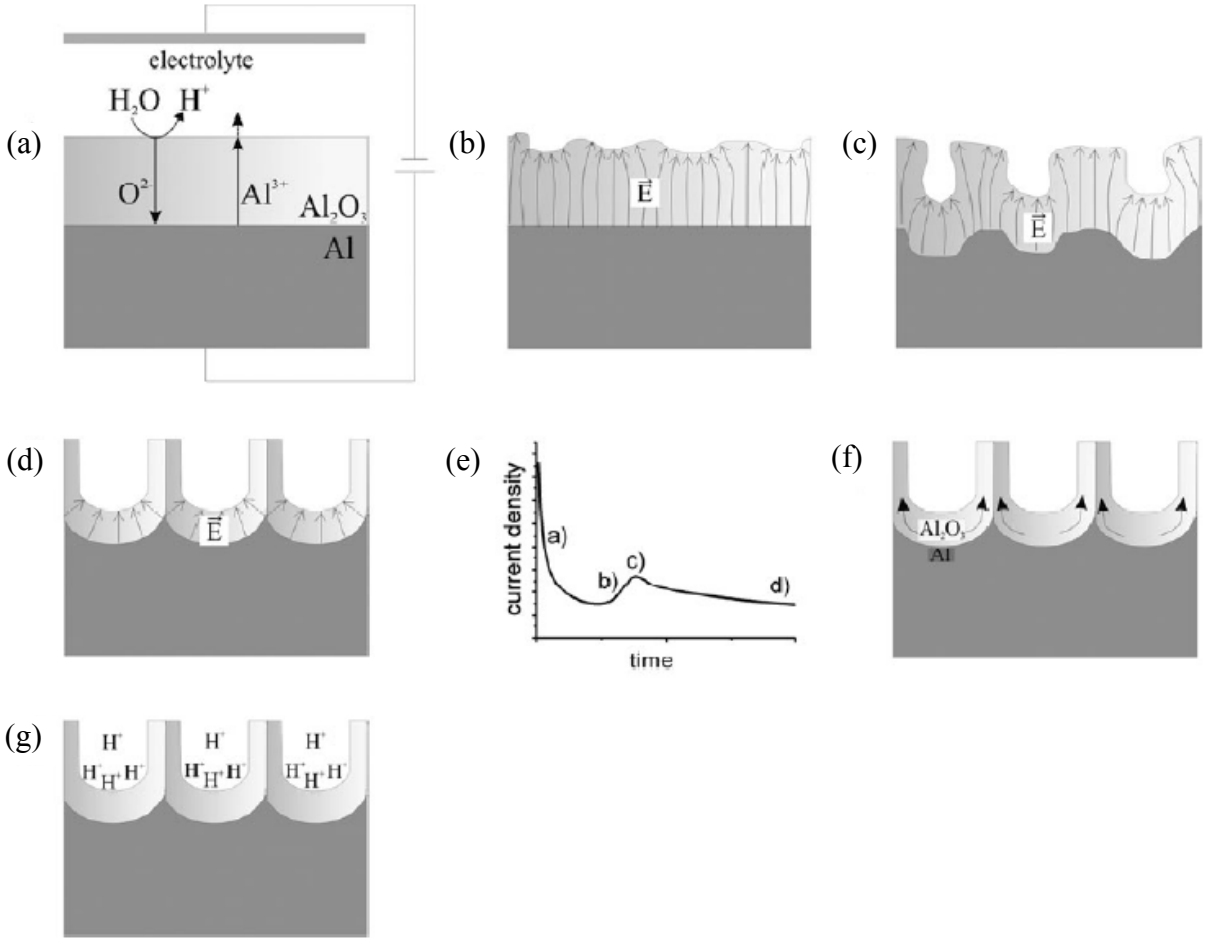

Figure 2.4 Schematic illustrations of the formation of alumina pore by anodization: (a) formation of the anodic oxide layer on aluminum, (b) local field distribution related to the surface morphological fluctuations, (c) initiation of the pore growth by field-enhanced dissolution, (d) pore growth under steady state conditions, (e) current density with time during anodization, (f) influence of volume expansion on pore growth, and (g) effect of local acidity on pore growth [25].

Then the pores start to be formed by the localized field-enhanced dissolution in the compact oxide layer, as illustrated in Figure 2.4 (c). The pores steadily grow to have a highly ordered

structure, as shown in Figure 2.4 (d). The current density with time shows the different stage of the growth process. The influence of volume expansion and local acidity on the pore growth is shown in Figure 2.4 (f) and 2.4 (g), respectively.

2.3.2 Controlling TiO_2 Nanotube Array Geometry

The geometries of anodic TiO_2 nanotubes including pore diameter and wall thickness can be tailored in a wide range. In general, the pore diameter is found to be linearly dependent on the applied anodic potential during the growth [42]. TiO_2 nanotube diameters from 10 nm to 250 nm can be achieved at the anodization potentials range 1-45 V in an HF/HP_3O_4 aqueous solution [42]. It is remarkable that self-organized structures are obtained even at the applied potential as low as 1 V, although the surface morphology shows a web like structure rather than a clear tubular morphology [43]. The tunable pore size makes the anodic TiO_2 nanotubes bear potential for applications where the tube diameter is required to be tailored for specific use.

The wall thickness of the anodic TiO_2 nanotubes is affected by the electrolyte temperature. This is due to the fact that chemical etching rate is dependent on the electrolyte temperature. It was reported that the wall thickness could be tailored in the range of 9 nm to 34 nm when electrolyte temperature is varied from 5 ℃ to 50 ℃ [44].

The duration of anodization time determines the length of the anodic TiO_2 nanotube arrays, if the other electrochemical parameters are kept constant. However, if the reactions reach a steady state condition between the tube growth at the bottom and the electrochemical dissolution at the top, no further tube growth in length is observed [25]. To increase the length of tubes, low dissolution rate is required, which can be carried out under low electrolyte acidity and low fluoride ion concentration. When the anodization is carried out in a non-aqueous

electrolyte or an organic solution with a small amount of water, the length of TiO_2 nanotube array keeps increasing.

2.3.3 Crystal Structures of TiO_2 Nanotube Arrays

When TiO_2 nanotubes are produced by anodization, they are typically amorphous form. Thermal treatment above 300 ℃ converts an amorphous form to anatase or a mixture of anatase and rutile. The three crystalline structures of TiO_2 are shown in Figure 2.5. Up until now, annealing treatments that lead to a complete conversion to rutile have not been achieved because it needs a high temperature. Annealing treatment at around 700 ℃ gives rise to considerable morphological deterioration such as sintering and collapse. When amorphous TiO_2 nanotubes are annealed in an oxygen ambient, the nanotube walls turn to anatase, while the barrier is converted to rutile [25].

The properties of anodic TiO_2 nanotube arrays depend heavily on their crystallization. Therefore, different phase TiO_2 is employed for a specific application. In general, anatase is preferred in charge separating devices such as QDSSCs and photocatalysis because anatase exhibits a significant higher charge carrier mobility than rutile [25]. This feature is very important in photoelectrochemical applications. The conversion of an amorphous nanotubular structure to anatase can be carried out by thermal annealing at temperatures between 300 ℃ to 500 ℃. The specific temperatures and annealing rates can change the resulting crystallite size as well as the tube morphology [25].

The different nanotubular structures show great difference in the photoresponse results. The strong enhancement of incident photon-to-current conversion efficiency (IPCE) is observed

after annealing as-prepared nanotubes. This is due to the fact that for the as-prepared amorphous structure most photocurrent is generated at the bottom of the nanotubes and the contributions of the nanotube walls are negligible due to a high carrier recombination rate resulting from numerous defects [25].

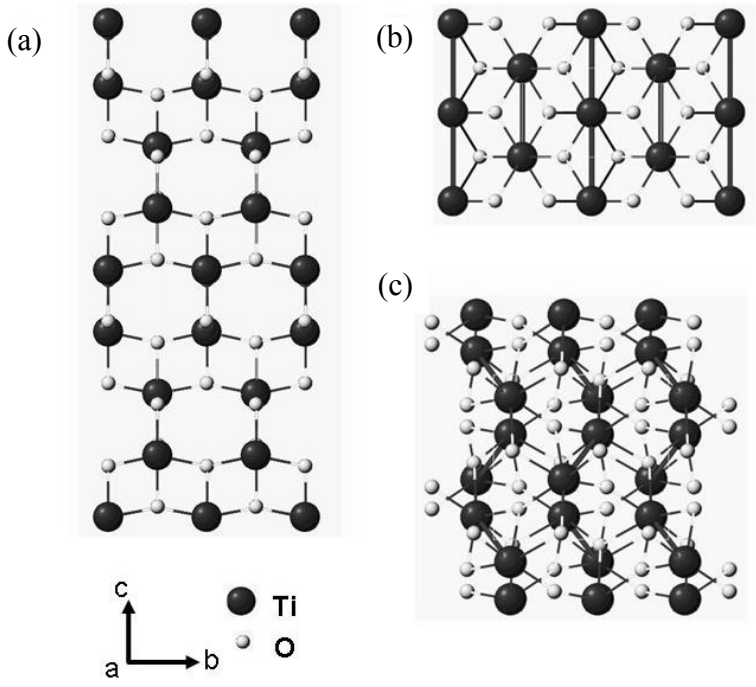

Figure 2.5 Three crystalline structures for TiO_2: (a) anatase, (b) rutile, (c) brookite. Symmetry and space groups for the polycrystalline: anatase (tetragonal, a = b = 3.782 Å, c = 9.502 Å), rutile (tetragonal, a = b = 4.584 Å, c = 2.953 Å), brookite (rhombohedral, a = 5.436 Å, b = 9.166 Å, c = 5.135 Å) [45].

Anodic TiO_2 nanotube arrays are expected to exhibit different photoelectrochemical properties compared to a nanoparticular TiO_2 layer. A low degree of distorted crystal structures at grain boundaries enhance electron scattering but reduce electron mobility. Smooth tube walls with a low surface state density reduce a surface recombination rate. The straight tube structure

reduces an extensive random path through a porous network in nanoparticular TiO_2 layers [25]. Although the effects of nanotube structures on the photoelectrochemical properties were intensively investigated, the optimized geometry of anodic TiO_2 arrays including length, diameter, and wall thickness for photoresponse is still limited.

2.4 Electrophoretic Deposition

2.4.1 Factors Influencing Electrophoretic Deposition

Electrophoretic deposition is one of the colloidal processes originally for ceramic layer production with a wide range of applications. In electrophoretic deposition, charged particles suspended in a liquid medium are attracted and deposited on a conductive electrode of opposite charge under an electric field. When particles are positively charged, the particles deposit on the cathode while negatively charged particles deposit on the anode. The principal driving force which enables charged particles to move is the charge on the particles. The electrophoretic mobility of the particles in the solvent is a main parameter influencing the driving force.

There are two groups of parameters which determine an electrophoretic deposition process. One group of parameters is related to the suspension and the other group is associated with the process including physical parameters such as the electrical nature of the electrodes, the electric field and deposition time. Suspension parameters are particle size, dielectric constant of liquid, conductivity of suspension, viscosity of suspension, and zeta potential. For particle size, there is no general rule to specify particle sizes suitable for electrophoretic deposition but it is important that particles remain completely dispersed and stable in a liquid solvent. The main problem for the larger particles is that they tend to settle down due to gravity. In addition, very strong charge on the surface of the particles is required or the electrical double layer region must

increase in size. In the liquid with too low dielectric constant, deposition can be unsuccessful because of insufficient dissociative power, while with a high dielectric constant the high ionic concentration in the liquid reduces the double layer region as well as the electrophoretic mobility. The conductivity of suspension needs to be taken into account because if suspension is too conductive, particle motion is very low and if suspension is too resistive, the charged particles lose stability. Therefore, there is a suitable range of conductivity for electrophoretic deposition but the range is different for different systems. The zeta potential of particles is a main factor in the electrophoretic deposition process. It is imperative to attain a high and uniform surface charge of particles because it plays a role in stabilization of the suspension by determining the extent of repulsive interaction between particles and the direction and migration velocity of the particles. A charged particle in a suspension is surrounded by ions with an opposite charge. The opposite charge ion layer can be divided into two parts. In the inner region, stern layer, the ions are strongly bound and in the outer region, diffuse layer, the ions are less firmly associated. Within the diffuse layer, there is a boundary inside which the ions and particles form a stable entity. When an electric field is applied, the ions within the boundary move along with the particle. Hence, the speed of a particle is not determined by the surface charge of the particle but by the net charge including the liquid sphere, which moves along with the particle. Those ions beyond the boundary stay with bulk dispersant. The potential at this boundary, surface of hydrodynamic shear, is zeta potential, as shown in Figure 2.6. The importance of the zeta potential is that magnitude of it indicates the potential stability of the colloidal system. If the all the particles in suspension have a large zeta potential, they will repel each other and they will not be prone to come together. In contrast, if the particles have a low zeta potential then there will be tendency for the particles coming together and flocculating. In general, zeta potentials more

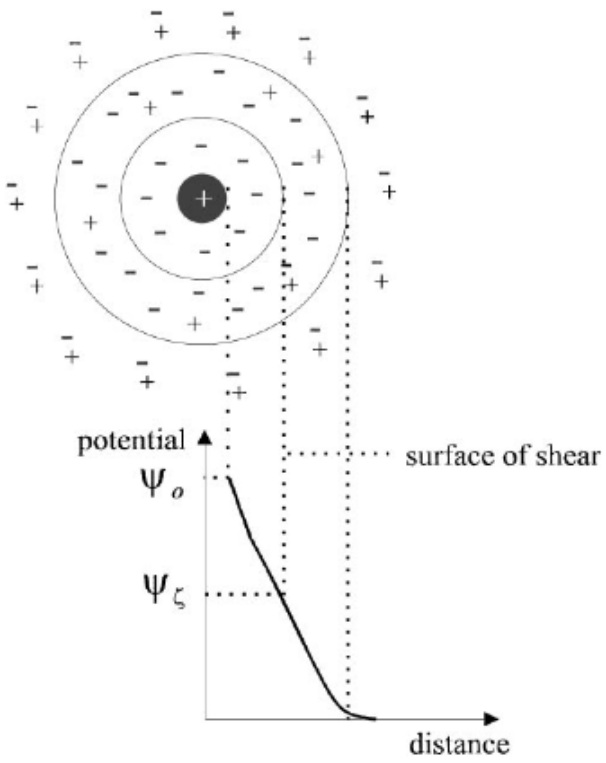

Figure 2.6 Schematic representation of the double layer surrounding a charged particle and evolution of the electric potential from the surface potential, Ψ_0, to zero far from the particle. The potential at the surface of shear, the limit of liquid moving with the particle is termed the zeta-potential, Ψ_ξ [46].

positive than +30 mV or more negative than -30mV are suggested for stable particles [46]. Zeta potential is affected by the pH of suspension, conductivity, and the concentration of a formulation component. pH is one of the most important factors that affect its zeta potential. When base or acid is added to suspension, particles in the suspension acquire more negative charge or positive charges. Therefore zeta potential versus pH curve will be positive at low pH and lower or negative at high pH [46]. Applied voltage is one of the critical parameters which are related with the process. Normally the amount of deposit increases as the applied voltage

increases. Although particles can be deposited quickly under the high electric field, the quality of the deposit can be degraded. An accumulation rate of particles affects their packing behavior in coating because the formation of particulate film is a kinetic phenomenon. For the higher applied field, the deposition may be disturbed by the turbulence in suspension. In addition, particles can move so fast that they cannot form a uniform or packed structure. Consequently, applied field influences a deposition rate and structures of deposit since applied potential exerts pressure on particle flux and movement. The amount of deposit increases with deposition time whereas deposition rate for a fixed electric field decreases with prolonged deposition time. Deposition is linear during the initial time of deposition but with time the deposition rate reduces [46]. In a constant voltage, this phenomenon is expected because electric field influencing electrophoresis decreases as the thickness of the insulating layer of particles on the electrode increases. The volume fraction of solid in suspension is important because particles could deposit at different rates depending on it [46]. When the volume fraction of solids is high, the particles deposit at an equal rate [46]. In contrast, when it is low, the particles can deposit at rates proportional to their individual electrophoretic mobility [46].

2.4.2 Kinetics of Electrophoretic Deposition

Knowledge of the kinetics of electrophoretic deposition is crucial in order to control a deposition rate and achieve flexibility in structural manipulation. The amount of deposit is proportional to the concentration of suspension, time of deposition, surface area of deposit, and applied electric field. Electrophoretic deposition can be conducted under a constant current or a constant voltage mode with either constant or decreasing the concentration of suspension with deposition time. As concentration of suspension decreases, a deposition rate decreases during

either a constant current or a constant voltage. Even if the concentration of suspension is kept constant during deposition, a deposition rate decreases under a constant voltage condition. This indicates that a decrease in particle velocity occurs as a function of deposition time. The deposited mass acts as a shielding effect and has higher electrical resistance than suspension, which reduces the electrical driving force or the voltage per unit length of suspension.

2.4.3 Mechanism of Electrophoretic Deposition Process

An electrophoretic deposition process consists of two steps, where charged particles migrate towards an electrode and they are deposited by a complex superposition of electrochemical and aggregation phenomena. The deposition mechanism can be explained by flocculation resulting from particle accumulation. The incoming particles generate pressure and enable the particles next to the deposit to overcome the repulsive force resulting from the same surface charge. It was reported that particles would be neutralized upon contact with the deposition electrode rather than become static [47]. This mechanism is important for monolayer deposition. It explains the initial stage deposition form but is invalid for thick layer deposition. Electrochemical particle coagulation mechanism implies a reduction of the repulsive forces between particles. An increase in ionic strength near an electrode reduces the interparticle repulsion [46]. The same order of ionic strength is required to flocculate a suspension. An increase in electrolyte concentration lowers zeta potential and induces flocculation of particles [46].

2.5 Quantum Dot Sensitized Solar Cells

2.5.1 Fundamental of Quantum Dot Sensitized Solar Cells

A constructed quantum dot sensitized solar cell (QDSSC) is schematically shown in Figure 2.7. The quantum dot sensitized solar cell consists of a quantum dot covered TiO_2 layer and an electrolyte. Transparent conductive oxide (TCO) is used as a counter electrode. Fluorine

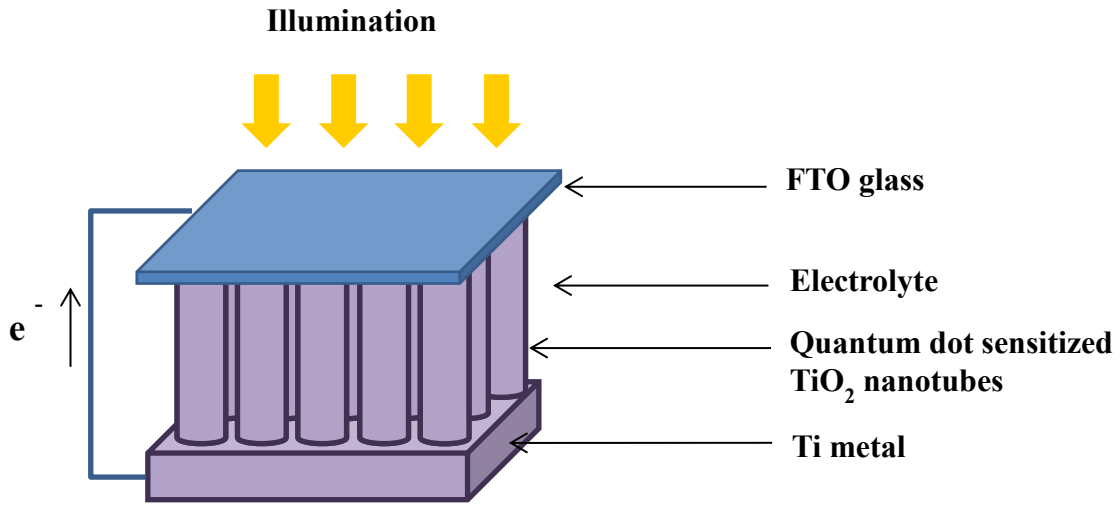

Figure 2.7 Schematic representation depicts a quantum dot sensitized solar cell based on TiO_2 nanotubes and electron path.

doped tin oxide (FTO) is most commonly used due to their high temperature tolerance. A few atomic layers of platinum are coated on the FTO in order to catalyze the redox reaction with an electrolyte. The anode is Ti metal on which TiO_2 nanotubes are located. Among three crystalline structures of TiO_2, anatase, rutile, and brookite, anatase is preferred due to the high carrier mobility. On the surface of the TiO_2 nanotubes, quantum dots are adsorbed. The huge nanoporous surface enables an adsorption of a sufficiently large number of quantum dots for

efficient light harvesting. Between anode and cathode, a liquid redox electrolyte is encapsulated. A liquid electrolyte has an advantage of being able to permeate into nanosize pores of TiO_2 tubes. The redox couple, iodide/triiodide (I^-/I_3^-), is commonly used. The ionic iodide liquid reacts with iodine (I_2) to form triiodide (I_3^-):

$$I_2 + I^- \rightarrow I_3^- \tag{2.11}$$

When the solar cell is in operation, the following redox reaction takes place:

$$I_3^- + 2e^- \rightarrow 3I^- \tag{2.12}$$

The energy diagram and electron transport path are shown in Figure 2.8. A mesoscopic semiconductor oxide TiO_2 has a large band gap of 3.2 eV, corresponding to a wavelength of λ = 390 nm. Thus, TiO_2 cannot absorb the visible light while it can absorb UV light. In order to absorb the visible light, InP quantum dots are attached to the TiO_2 layer. InP quantum dot energy band gap depends on the size of the quantum dot but it can be assumed to be approximately 2.0 eV based on the typical size of the synthesized InP quantum dots. Due to the small band gap, the quantum dots absorb photons from the visible light and generate excited electrons. The excited electrons are rapidly injected into the conduction band of the TiO_2 because the TiO_2 conduction band is lower than that of InP quantum dots. Thus, the InP quantum dots have a large driving force for injecting the photogenerated electrons into the TiO_2. The electrons in the conduction band are transported to the FTO electrode, actually Ti metal in case of this work, by diffusion of the electrons. In conventional p-n junction, photogenerated charges are separated by the electric field in the space charge region. In QDSSCs, however, the individual particle size is so small that

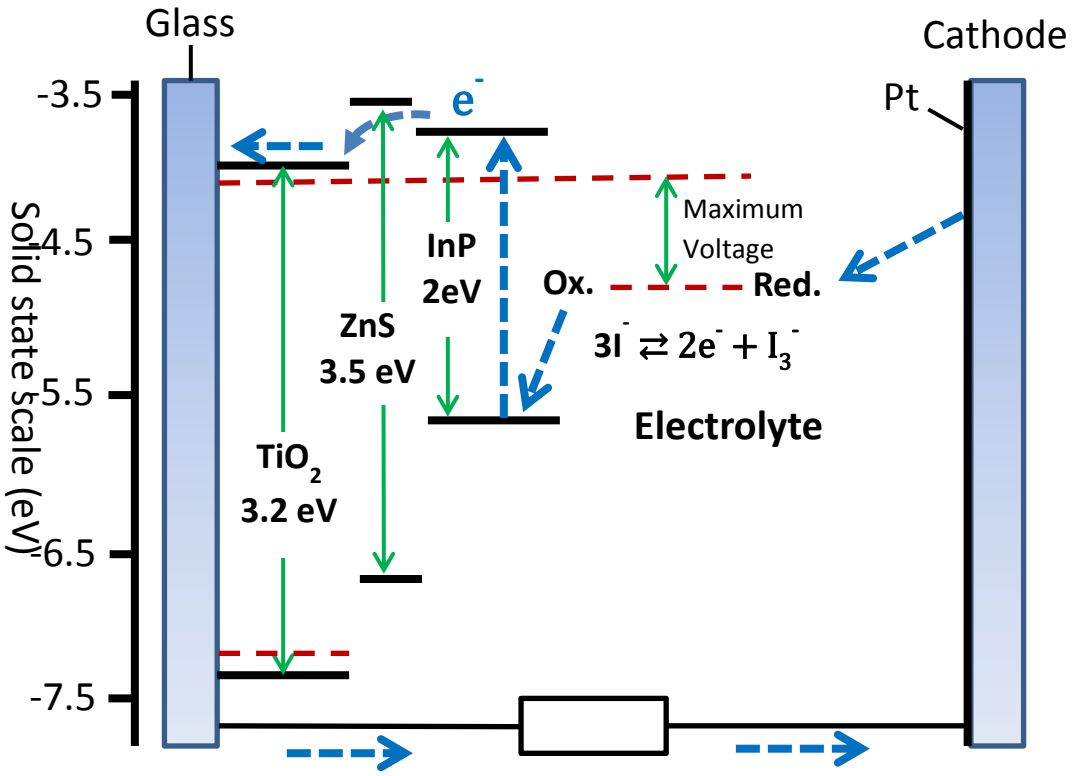

Figure 2.8 Schematic operation of InP/ZnS quantum dot sensitized TiO_2 solar cell is shown.

space charge region cannot form [48]. In addition, electrons in the electrode are screened by cations, the counter charges of I^-/I_3^- redox couples in the electrolyte, which does not give rise to potential gradient in the electrode [48]. The oxidized sensitizers, quantum dots, are reduced by I^- ions. The I_3^- ions diffuse toward the counter electrode and are then reduced to I^- ions.

2.5.2 Basic Principles of Solar Cells

Sunlight is a radiation spectrum of photons distributed over a range of energy. Just above the Earth's atmosphere, the radiation intensity is about 135.3 mW/cm^2 and this spectral

distribution is referred to as air mass zero (AM0). The air mass is a measure of how angle of incidence affects the intensity of the solar radiation reaching the Earth's surface. The air mass Number is given by [49]:

$$\text{Air mass} = \frac{1}{\cos\theta} \tag{2.13}$$

Where θ is the angle of incidence on the Earth's surface. A widely used standard for comparing solar cell performance is the AM1.5 (θ = 48.2 °) corresponding to a total power density of 100 mW/cm^2.

The current voltage (I-V) characteristic curves by an ideal diode can be written as:

$$I = I_0 \left[\exp\left(\frac{qV}{nkT}\right) - 1\right] \tag{2.14}$$

Where, I is the current, I_0 is the saturation current, q is the charge, k is the Boltzmann constant, T is the temperature and n is the ideality factor of the diode. With no light on a solar cell, it behaves as a normal p-n junction diode and follows the equation 2.14. The generated current is called dark current. Under illumination electron hole pairs are generated, called photocurrent. The illumination adds additional current in reverse direction to the dark current and the diode equation becomes

$$I = I_L - I_0 \left[\exp\left(\frac{qV}{nkT}\right) - 1\right] \tag{2.15}$$

Where, I_L is the photocurrent. I-V curves and equivalent circuits of a p-n junction in dark and light condition are shown in Figure 2.9. The current at which the voltage is zero is short circuit current, denoted by I_{sc} and the voltage at which the current becomes zero is open circuit voltage,

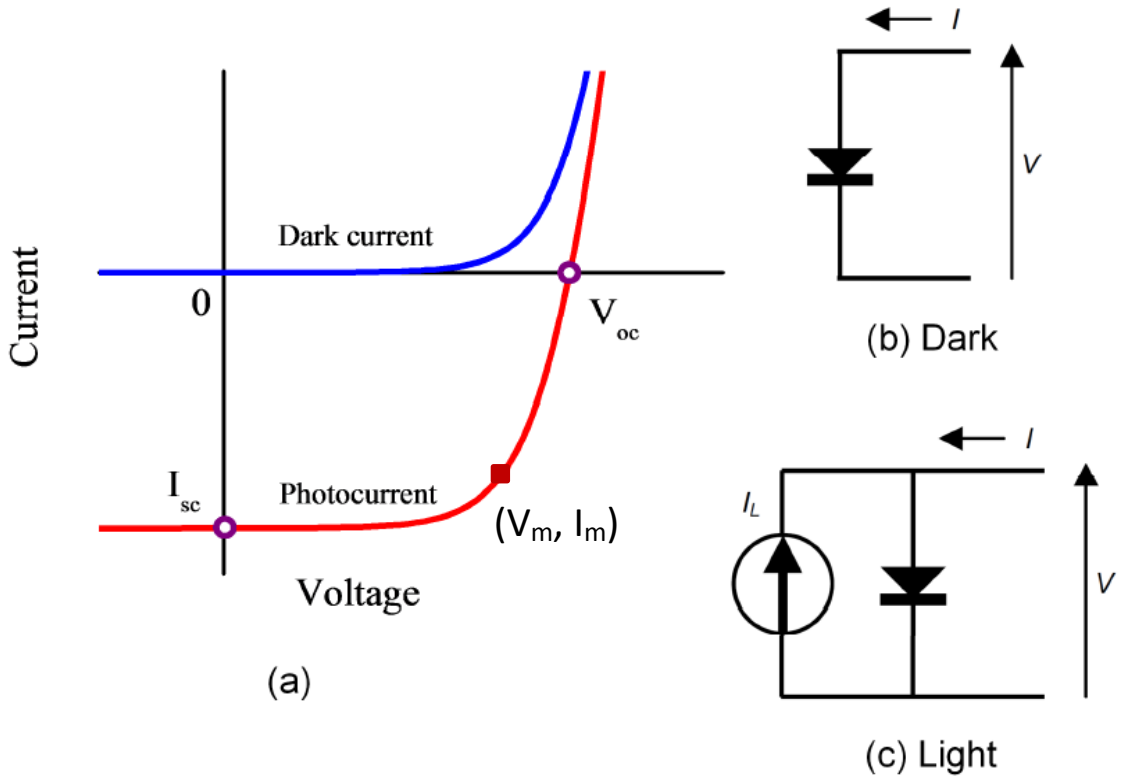

Figure 2.9 (a) I-V characteristic of a solar cell under illumination shows the maximum power point. (b) A p-n junction circuit in dark condition. (c) A p-n junction equivalent circuit under light irradiation.

denoted by V_{oc}. The maximum power point is determined by a square in Figure 2.9 (a) and the voltage and the current at the maximum point are denoted by V_m and I_m respectively. The performance of solar cells are evaluated by the two main factors, which are fill factor (FF) and power conversion efficiency (η). The physical meaning of fill factor is associated with the

junction quality and parasitic resistance of the cell. The closer the fill factor is to unity, the higher the quality and efficiency of a solar cell is. Fill factor and power conversion efficiency are given by the following equations:

$$FF = \frac{V_m I_m}{V_{oc} I_{sc}} \tag{2.16}$$

$$\eta = \frac{V_m I_m}{P_{input}} \times 100\ \% = FF\ \frac{V_{oc} I_{sc}}{P_{input}} \times 100\ \% \tag{2.17}$$

The efficiency of a solar cell depends on the band gap of it. Therefore, there is the optimum band gap for maximum power generation at a solar radiation of AM1.5 and it is found to be 1.5 eV [50]. In general semiconductors with a band gap in the range of 1.0 ~ 1.7 eV are suggested for solar cell applications [51].

3. CHARACTERIZATION TECHNIQUES

3.1 Material Characterization

3.1.1 Microscopies

Scanning electron microscopy (SEM) and transmission emission microscopy (TEM) are widely used to probe the morphology of nanostructures. SEM is a type of electron microscope, directing an electron beam to a target by using electromagnetic fields and then measuring the interaction of those electrons with the target at a detector. The signals that derive from electrons and a target sample reveal information about the sample including external morphology, crystalline structures, and orientation of materials. Accelerated electrons in an SEM carry substantial amounts of kinetic energy, and the energy is dissipated as many kinds of signals produced by electron-sample interactions when the incident electrons are decelerated in a solid sample. Secondary and backscattered electrons produce SEM images. Diffracted backscattered electrons are used to determine crystal structures and orientation of materials. Photons produced by inelastic collisions of the incident electrons with electrons in discrete orbitals of atoms generate X-rays, which are used for elemental analysis. SEM analysis is considered to be non-destructive. No volume loss of sample makes it possible to analyze the same material repeatedly.

Transmission emission microscopy (TEM) uses high energy electrons up to 300 kV, which are accelerated to nearly the speed of light. When an electron beam passes through a specimen of a material, electrons are scattered. A sophisticated system of electromagnetic lenses detects the scattered electrons and produces an image or a diffraction pattern, or a nano-analytical spectrum. The image provides a highly magnified view of nanostructure and high

resolution image provides a direct map of atomic arrangements. The diffraction pattern displays accurate information about the local crystal structure.

3.1.2 X-ray Diffraction

X-ray diffraction (XRD) is a material characterization technique to determine the atomic and molecular structure of a crystal. Crystalline atoms cause an incident beam of X-rays to diffract into many specific directions. By measuring the angles and the intensities of these diffracted beams, the density of electrons within the crystal is obtained. This electron density determines the crystal structure and its orientation, and elements. The produced TiO_2 nanotubes were measured using Philips PW 3040 X'PERT MRD High Resolution XRD. Different crystalline structures of the TiO_2 nanotubes were studied with varied annealing temperatures.

3.1.3 Ultraviolet-Visible Spectroscopy

An ultraviolet-visible (UV-Vis) spectrophotometer is a device which measures the absorbance, reflectance, and transmittance. In this project, a Cary 500 UV-Vis spectrophotometer, which is shown in Figure 3.1, was used to measure the absorbance of InP/ZnS nanocrystals suspended in hexane. A quartz cuvette with optical path of 10 mm is used.

Absorbance is a measure of the loss of light due to scattering and absorption when it passes through a medium. In the Cary 500 UV-Vis spectrophotometer, incident light intensity and transmitted light intensity are detected, producing the absorbance of a sample. Therefore, an absorbance result includes the two effects of scattering and absorption on the attenuation of a light beam.

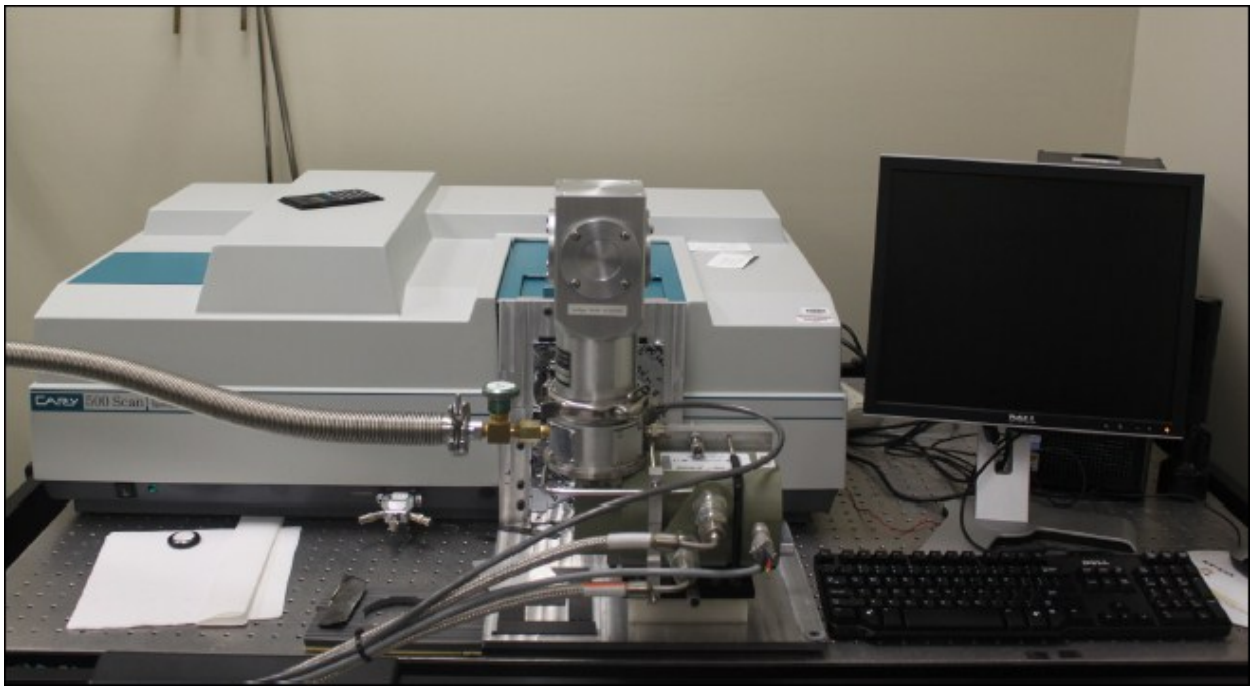

Figure 3.1 Cary 500 UV-Vis spectrophotometer for measuring absorbance.

Absorbance is given by:

$$A = -\log T = -\log\left(\frac{I}{I_0}\right) \tag{3.1}$$

Transmitted light intensity can be written as:

$$I = I_0 \exp(-\alpha \ell) = I_0 \exp(-C_{ext} \ell N) \tag{3.2}$$

Where I is transmitted light intensity, I_0 is incident light intensity, T is transmission, α is absorption coefficient, C_{ext} is extinction coefficient of nanoparticles, ℓ is the optical path length (cuvette width) through the solution, and N is the nanoparticle concentration.

4. EXPERIMENTAL

4.1 Synthesis of InP/ZnS core/shell Nanocrystals

The growth started by synthesizing indium(III) precursors. Indium acetate $In(Ac)_3$ (10 mmol) was mixed with myristic acid (40 mmol) and heated to 140 ℃ under a nitrogen atmosphere. The mixture was heated for 6 hours and then isolated by adding acetone. The product was filtered and dried. Myristic acid was again added to the product to make sure complete conversion of acetate to myristate. The final product, indium myristate $In(Mt)_3$ was washed with acetone to remove any remaining myristic acid, dried and used as an indium precursor. Three synthesis methods were performed in order to have InP/ZnS nanocrystals covering the UV to the near infrared: A one pot reaction, the complete growth of the InP core before the ZnS shell growth, indium precursor and InP/ZnS nanocrystals *in situ* synthesis including the growth of InP core before ZnS shell growth. First the one pot reaction, which is relatively simple and convenient, was carried out. All precursors indium myristate [$In(Mt)_3$] (2 mmol), tris(trimethylsilyl)-phosphine [$P(TMS)_3$] (1 mmol), and dodecanthiol [DDT]) (2 mmol), zinc stearate (4 mmol) were mixed in 1-octadecene (ODE) under nitrogen at room temperature and subsequently heated to 300 ℃ within 10 min. One pot reaction was also carried out in terms of reaction time to tune InP core size. The method of complete growth of the InP core before the ZnS shell was aimed to separate the shell growth from the core growth. ZnS shell was grown after the growth of InP core at different temperatures 180, 250 and 300 ℃. For the growth of ZnS shell, the reaction solution was cooled down to 150 ℃. Zinc stearate (2 mmol) and DDT (1 mmol) were subsequently added to the InP nanocrystals in the reaction flask, waiting for at least 10 min between each injection at 150 ℃. After that, the temperature was increased to 230 ℃ for 30 min,

in order for DDT to react. The decomposition temperature of pure DDT is 350 ℃; however, the presence of other compounds within the reaction mixture causes the decomposition temperature of DDT to drop to around 230 ℃, releasing sulfur for the formation of the ZnS shell [52]. For *in situ* synthesis of indium precursor and InP/ZnS nanocrystals, $P(TMS)_3$ was added to the flask including as-prepared $In(Mt)_3$ and reacted *in situ*. ZnS shell was then grown on the InP core. Furthermore, to study the effect of the injection temperature, the phosphorus precursor was injected at temperatures 100 ℃, 200 ℃ and 300 ℃. Synthesis of InP/ZnS nanocrystals was followed by a purification step. Hexane and methanol were added to the reaction solution. The InP/ZnS nanocrystals are dissolved in hexane while ODE solvent and unreacted compounds are dissolved in methanol. By the successive methanol extraction, pure InP/ZnS nanocrystals were obtained in hexane. For applications of InP/ZnS nanocrystals, a solution deposition technique was tested. Dithiol was used as a linker between InP/ZnS layers. The UV-Vis absorbance was measured as a function of the number of layers.

4.2 Growth of TiO_2 Nanotubes

For TiO_2 nanotube growth, titanium foil was cleaned with acetone, ethanol, and deionized water. It was subsequently dried off with nitrogen gas. Electrochemical anodization of titanium was performed in a two-electrode configuration. The titanium foil was connected to positive charge to serve as the working electrode and a platinum foil was connected to negative charge to serve as the counter electrode. The anodization experiments were performed in an ethylene glycol solution containing ammonium fluoride and deionized water under the applied voltage of 50 V. The effect of the ratio between ammonium fluoride and deionized water on TiO_2 structure was investigated. The grown TiO_2 nanotubes were immediately rinsed with deionized water and

dried with nitrogen gas. The morphology and structure of nanotubes were observed by SEM. The as-grown TiO_2 nanotubes were annealed at 400 and 500 ℃ for 2 hours in air.

4.3 Electrophoretic Deposition

To couple the InP/ZnS nanocrystals with the TiO_2 nanotubes, an electrophoretic deposition method was carried out. A titanium foil with nanotubes was connected to the positive electrode and a platinum foil was connected to the negative electrode. The two electrodes were dipped into a flask filled with a nanocrystal containing hexane solution. The electrodes were connected to a dc power supply and 200 ~ 50 V were applied between the two electrodes, which were separated by 2 mm. The current was measured as a function of deposition time. The deposition results were observed by the measurement of TEM and energy-dispersive X-ray spectroscopy (EDX).

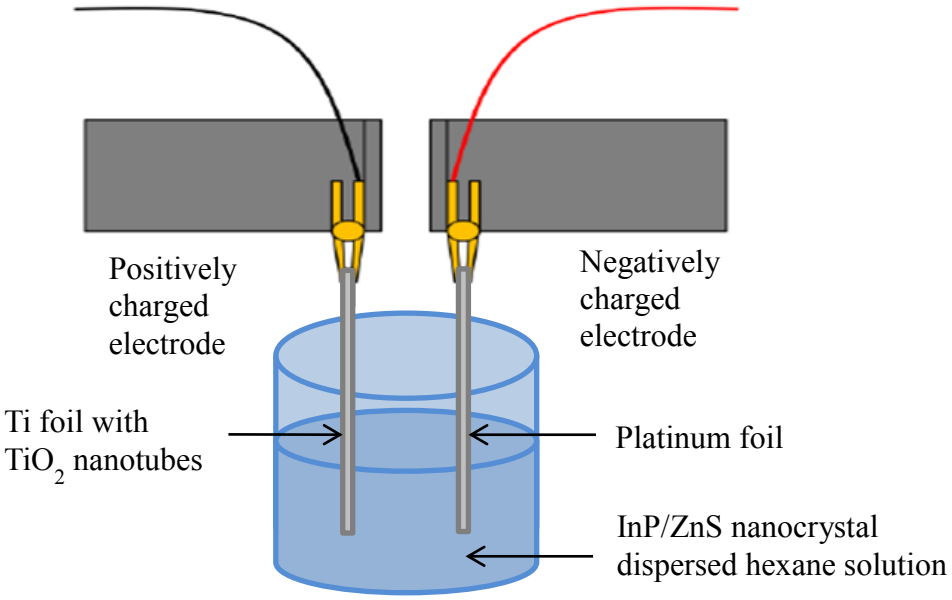

Figure 4.1 Electrophoretic deposition equipment with two electrodes spaced at a set distance.

5. RESULTS AND DISCUSSION

5.1 InP/ZnS core/shell Nanocrystals

5.1.1 Synthesis and Characterization

This research was focused on synthesizing InP/ZnS core/shell nanocrystals covering the UV to the near infrared. Especially, InP/ZnS nanocrystals with a relatively small bandgap close to the near infrared, which can be coupled with TiO_2 nanostructures to produce solar cells with high conversion efficiency. The research was conducted to synthesize broad size range of InP/ZnS nanocrystals. In order to control InP core size, reaction time was considered as a controlling factor in one pot reaction. Figure 5.1 shows as the reaction time increases, until it reaches 120 min, the emission and absorbance peaks shift to longer wavelength, indicating different size distribution of InP cores. This result implies that the nucleation step is immediate and fast whereas the growth step is slow. By taking this advantage, controlled size distribution of nanocrystals was prepared. For the one pot reaction, the *in situ* formation of the core/shell structure is ascribed to the difference in reactivity of the InP and ZnS precursors [53]. The reaction goes through several stages. In the first stage, highly reactive $P(TMS)_3$ is decomposed and InP core is formed. Once the growth of ZnS shell on the InP core starts, the incorporation of P into the nanocrystal stops, whereas the In content continues to increase. Therefore, InP core grows until the temperature reaches around 230 ℃ at which DDT starts to decompose, releasing sulfur [52]. During this process, color change is observed, from yellow to green and finally orange or dark red. This color change occurs during several minutes. Once the ZnS shell starts to deposit on the InP core, only In can diffuse into the ZnS. The InP are still growing but the growth rate becomes slow [52]. After 120 min the InP core growth rate is too slow to observe

red-shift. This slow rate limited further growth of the InP core. The longest fluorescence emission wavelength of the nanocrystals obtained by the one pot reaction was 560 nm. Even after 300 min, noticeable red-shift was not observed.

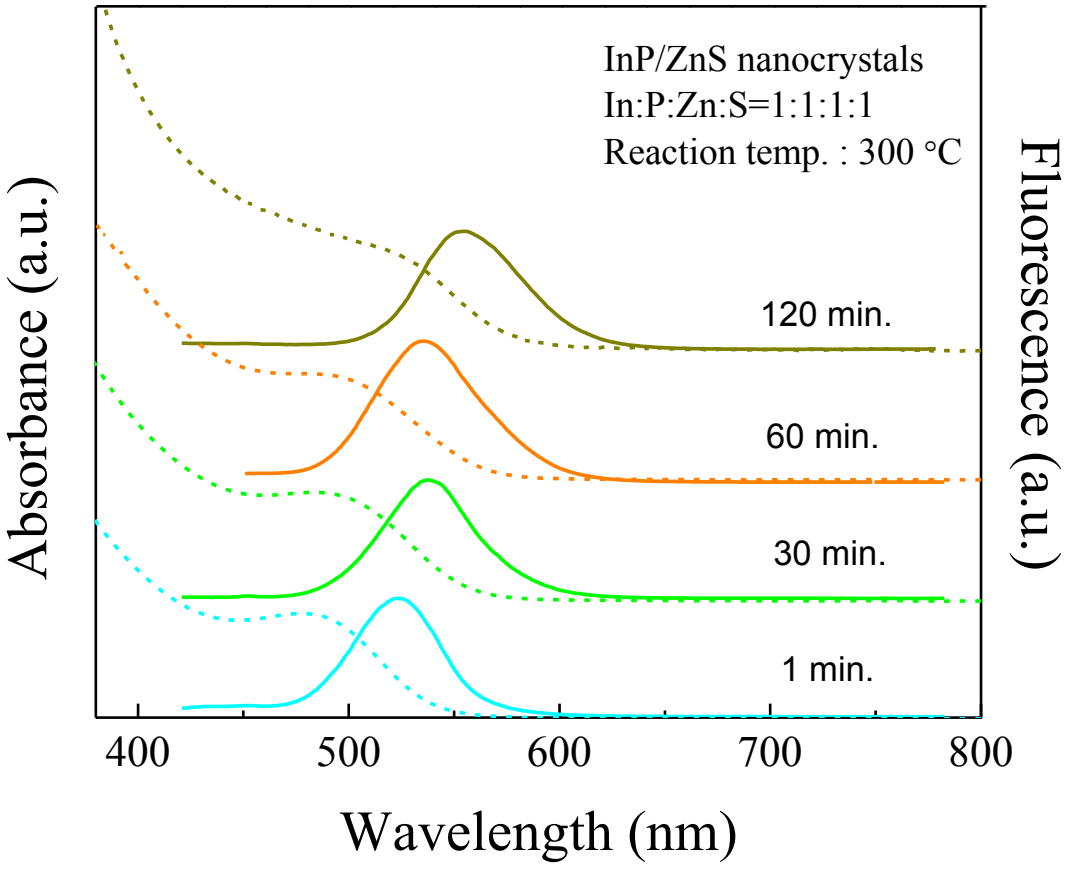

Figure 5.1 UV-Vis absorbance and emission spectra of InP/ZnS nanocrystals synthesized in the one pot method with reaction time (dashed line: absorbance, straight line: fluorescence).

In order to increases InP core size larger than the ones obtained from the one pot reaction, the ZnS shell growth step was carried out after the growth of InP core is complete. The InP core growth was performed with time varying from 120 min to 300 min. The emission peaks of the InP core with different growth time were detected around 580nm.

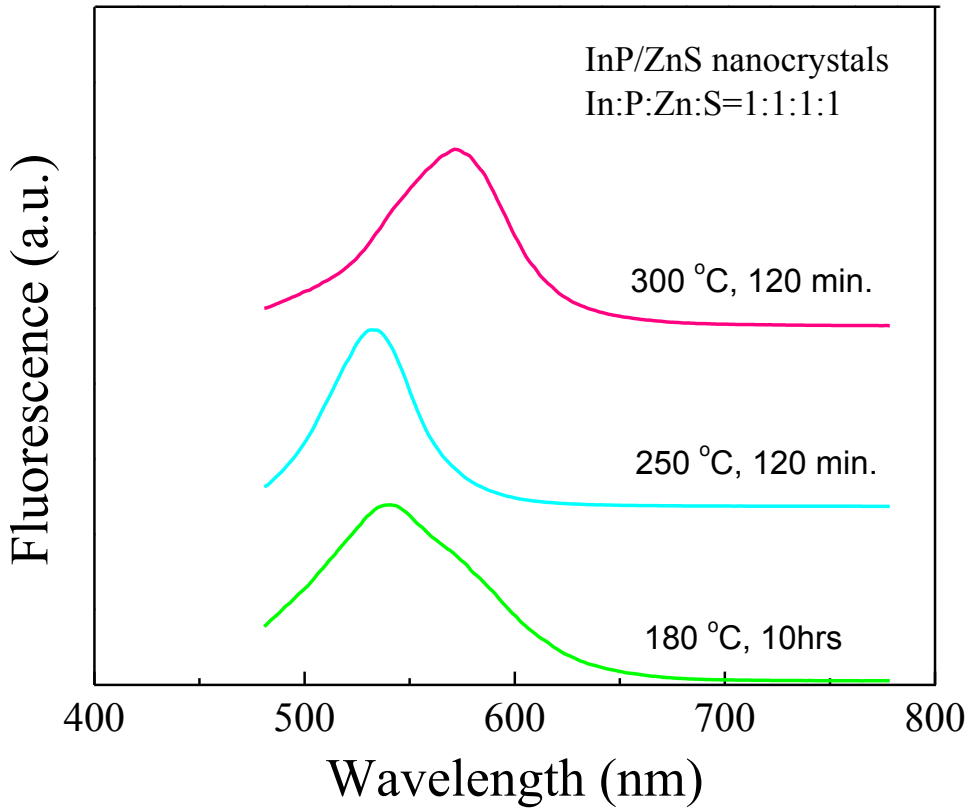

Figure 5.2 Emission spectra of InP/ZnS nanocrystals synthesized at different reaction temperatures.

Unexpectedly, even the separation of the two steps, InP core growth and ZnS shell growth, did not give significant red-shift. This result strongly supports the hypothesis of InP nanocrystal surface passivation by oxidative condition. During the reaction unexpected dialkyl ketone is formed by indium carboxylate precursor and this causes oxidation on the InP nanocrystal surface. The deactivated surface can hardly go through the ripening process. As a result, there is high possibility to prevent further growth of the InP core [54]. Reactions in this synthesis scheme were run at different temperatures 180 ℃, 250 ℃ and 300 ℃. At 250 ℃ and 300 ℃ reaction ran for 120 min and at 180 ℃ reaction lasted for 10 hours as shown in Figure 5.2. This result also shows that higher reaction temperature leads to red-shift, suggesting that the higher the reaction temperature, the bigger the size of the resulting InP core.

For the purpose of more red-shifted nanocrystals by reducing the oxidative condition, indium precursor $In(Mt)_3$ was prepared in the flask and subsequently the synthesis was performed *in situ*. After the growth of the core, the ZnS shell was grown. This scheme allowed InP core to grow further and the emission peak to go over 600 nm. From this result, it has become evident that oxygen causes the passivation on the surface of InP nanocrystals and prevents further growth of the core. Figure 5.3 shows different emission and absorbance peaks in terms of the three different synthesis schemes, even under the same reaction conditions.

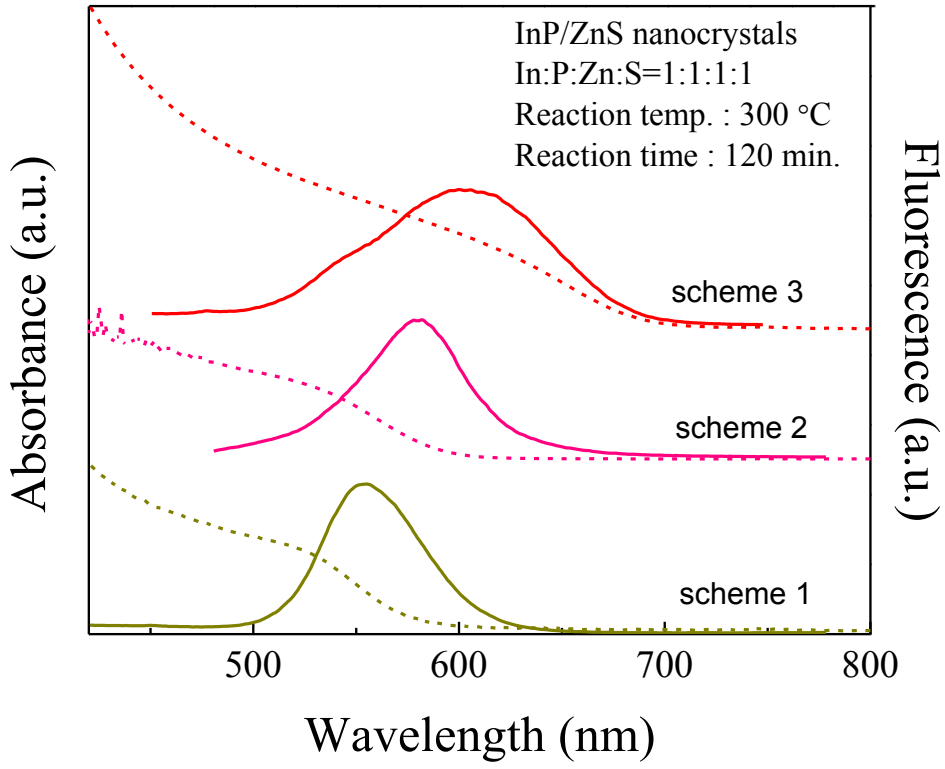

Figure 5.3 Emission and absorbance spectra in terms of different synthesis schemes (scheme 1: one pot reaction, scheme 2: complete growth of the core before the shell growth, scheme 3: indium precursor and InP/ZnS nanocrystals *in situ* synthesis and complete growth of the core before the shell growth, dashed line: absorbance, straight line: fluorescence).

To investigate the effect of different injection temperature, phosphorus precursors were injected at 100, 200 and 300 ℃ respectively into the flask filled with indium myristate solution in ODE. In case of the injection at 200 and 300 ℃, InP/ZnS nanocrystal product yield decreased dramatically. When the temperature was around 200 ℃, the color of the indium precursor solution turned yellow, which indicates that indium carboxylates were oxidized to form In_2O_3 due to the high activity of hydrolysis of indium carboxylates. Even when the experiment was performed with thorough degassing of the solution, the color change was still observed at around 200 ℃.

The photograph in Figure 5.4 shows diverse color from blue to red under UV light, implying a different emission wavelength of each sample as a result of the varied InP core size which was obtained by the synthesis methods mentioned above.

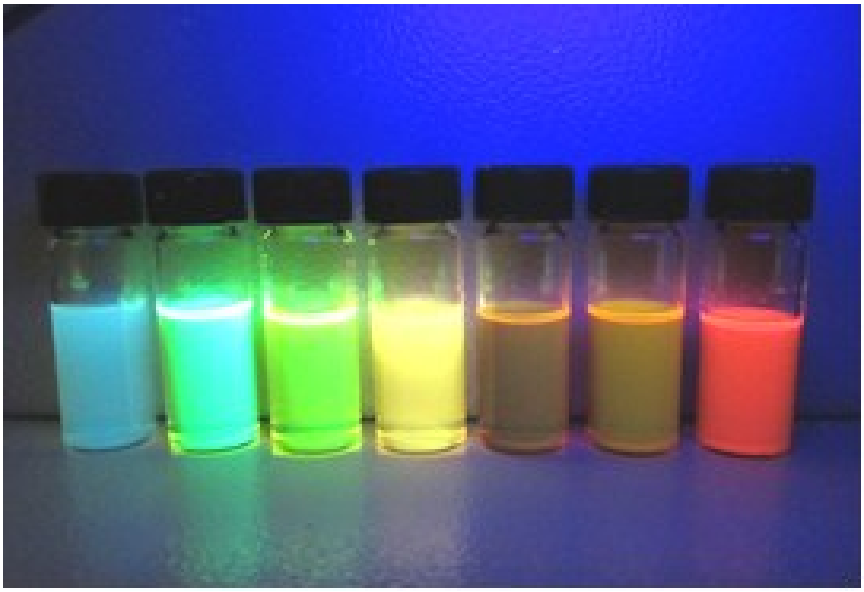

Figure 5.4 A photograph of InP/ZnS core/shell nanocrystal samples emitting from blue to red is shown.

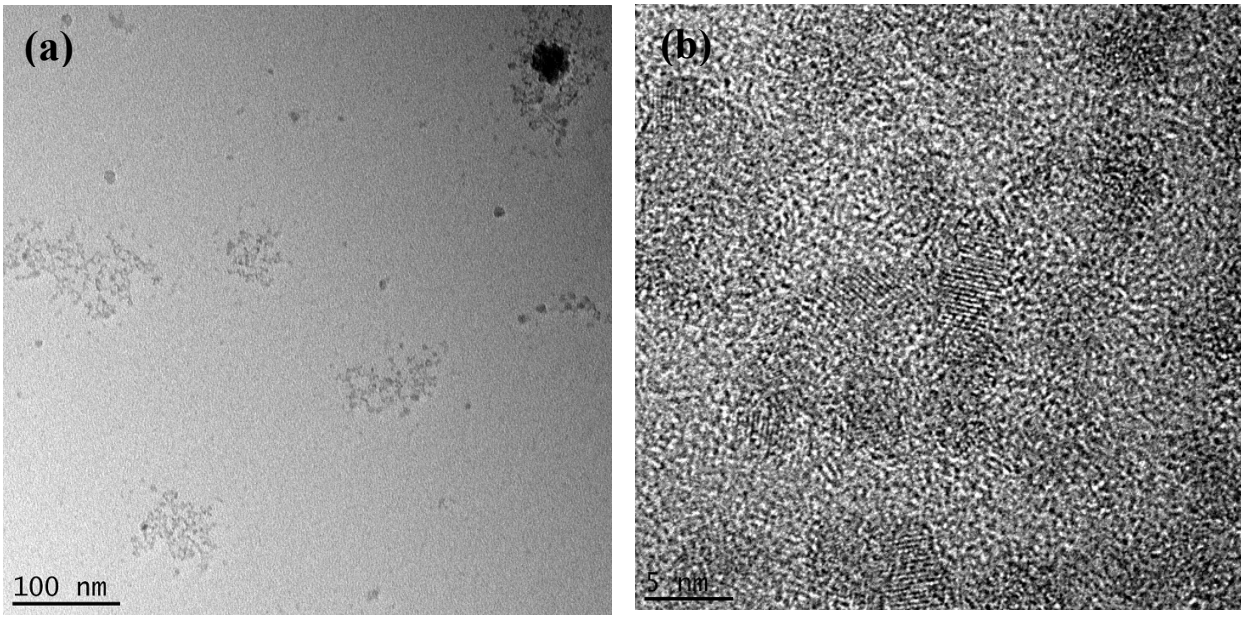

Figure 5.5 InP/ZnS nanocrystals are observed (a) in a low resolution TEM image and (b) in a high resolution TEM image.

One serious problem of InP nanocrystal is air instability in terms of oxidation. With time, nanocrystal absorbance spectrum shifts considerably to blue due to the shrinkage of the InP core by oxidation [52]. In order to solve this problem ZnS shell was grown on the InP core in our experiments. Absorbance and emission measurement was carried out several times for the same sample as the function of collapsed time. There was no shift of the absorbance and emission peaks, which indicates firm air stability. The average InP core is estimated about 5 nm from Figure 5.5 (b). ZnS Shell is hardly observed in the high resolution TEM image, so that it is expected to be very thin compared to the InP core. The bandgap of ZnS is much larger than InP, which can lead to strong confinement. However, the electron affinities of ZnS and InP do not differ much (3.9 and 4.4 eV respectively), so that the conduction band are very close to each other. These two aspects, very thin shell and close conduction band edges, are expected to cause

weak confinement in the InP core. This can facilitate that excited electrons in the InP conduction band readily tunnel through the ZnS shell. Consequently, these InP/ZnS core/shell nanocrystals are expected to be an optimized sensitizer for quantum dot sensitized solar cells.

5.2. TiO_2 Nanotubes

5.2.1 Morphological Aspect

In general, self-organized TiO_2 nanotubes are formed by anodization of Ti in electrolyte that contains fluoride ion. In this project, the anodization growth was carried out under varied conditions. The concentration of fluoride ion and the amount of deionized water were the controlling parameters to form a vertically oriented tubular structure. This feature has advantages of higher electron mobility as well as less interface recombination [55]. Two types of TiO_2 nanotubes, free-standing form and nanoporous form are shown in Figure 5.6.

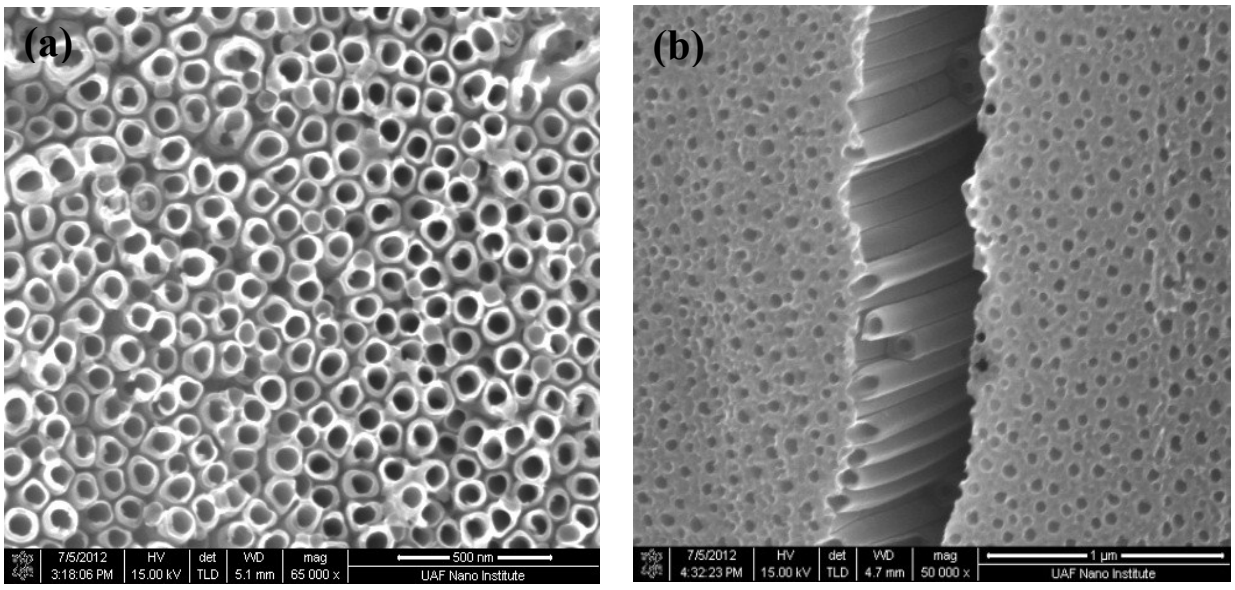

Figure 5.6 SEM images of (a) free-standing TiO_2 nanotubes and (b) nanoporous TiO_2 nanotubes.

The free-standing TiO_2 nanotubes were grown under the condition of ammonium fluoride 0.17 wt % and deionized water 1.7 wt % at 50V. The nanoporous form was obtained with ammonium fluoride 0.17 wt % and deionized water 0.4 wt % at 50 V. For the first step of TiO_2 nanotube formation, oxide layer is formed on the Ti metal. Ti^{4+} that is oxidized at the Ti metal-oxide interface migrate outwards under the applied field and react with O_2^- ions generated from

the water to form TiO_2 film. The thickness of the oxide film reduces the field strength, so that the growth rate of oxide film slows down [25]. Therefore, the thickness of oxide film can be controlled by the applied voltage level. The formation of nanotube arrays in a fluoride containing electrolyte results from field assisted oxidation of Ti metal to form titanium dioxide and chemical dissolution of titanium dioxide due to etching by fluoride ions [25]. The nanotube growth is determined by the equilibrium between the anodic oxidation and the chemical dissolution. The oxidation rate is determined either by the amount of water or anodic potential, while the chemical dissolution rate is determined by fluoride concentration. The highly ordered nanotubes in the SEM image indicate that the oxidation rate and dissolution rate were at the equilibrium under the growth conditions described above. In order for TiO_2 nanotubes to grow vertically, it is essential that the growth be carried out at the equilibrium with optimized applied voltage, water content, and fluoride concentration. The free-standing tubes shown in Figure 5.6 (a) were formed when the chemical dissolution speed associated with fluoride concentration is faster than the speed of Ti oxidation. In comparison, the nanoporous tubes were produced when the dissolution speed was slightly larger than the oxidation under the condition of decreased deionized water content. This is due to the fact that the increasing water content in the fluoride ion containing electrolyte increases the mobility of fluoride ions, inducing a significant increase in chemical dissolution at the top of the nanotubes. Although the growth of tubes is accelerated at the bottom of the tubes due to the increased water content, overall growth rate decreases because the dissolution of the top increases much faster than the growth.

In order to investigate the influence of the water content, the experiments were carried out with the increased water content of 4 wt % under the other parameters being unchanged. It is observed that the thickness of tube walls is very thin, as shown in Figure 5.7 (b). The diameter of

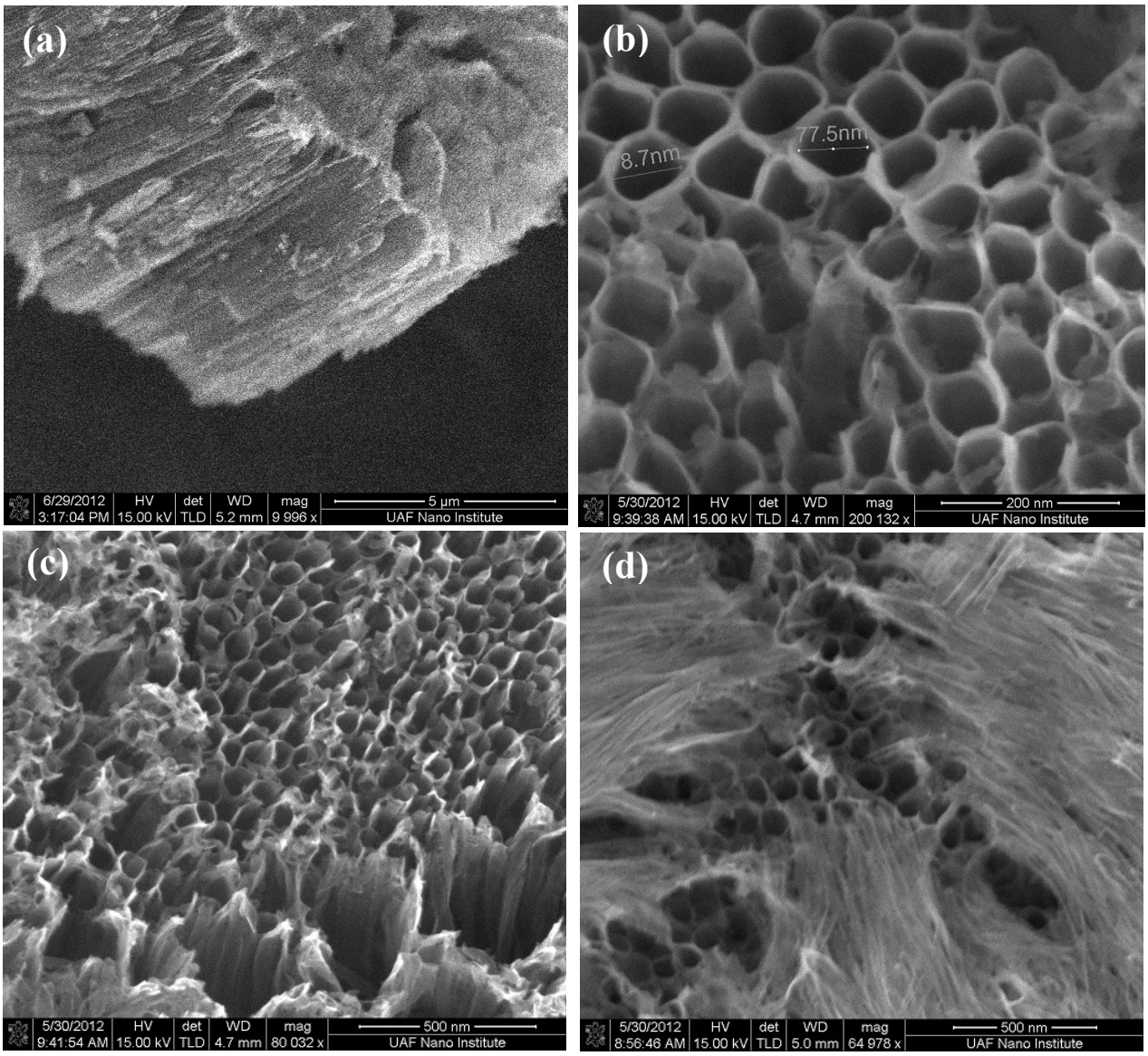

Figure 5.7 SEM images of anodic TiO_2 nanotubes grown in fluoride ion containing ethylene glycol: (a) cross-sectional view (b) top view (c) deteriorated tube top structure (d) tube top covered with remnants.

the tubes is increased, about 78 nm in Figure 5.7 (b), due to the thinner wall thickness, while the extensive dissolution reaction resulting from the increased water content deteriorates the tube structures. The tube walls are thinned out, perforated, as shown in Figure 5.7 (c) and even the

tube tops are covered with tube wall remnants, as shown in Figure 5.7 (d). It is apparent that this degraded structure will have negative effects on the carrier mobility and the deposition of the nanocrystals, ending up decreasing the solar cell efficiency. It is considered that the diameter of the tubes with relatively thick walls, about 70 nm in Figure 5.6 (a), is enough to deposit the synthesized InP/ZnS nanocrystals on the nanotubes due to the nanocrystal size is around 5 nm in diameter.

In this project, fluoride ions were used for the dissolution of oxide. A key feature of the fluoride ions is that they have the small ionic radius, which enables them to enter the growing tubes and to be transported to the metal-oxide interface for the chemical dissolution of the formed TiO_2. The other advantage of the fluoride ions is that they react with TiO_2 and form TiF_6^{2-} water-soluble complex. The use of fluoride ions is very significant for the optimized nanotube structure to fabricate solar cells because the formed TiO_2 layer at the interface can be thinned, resulting in an increase in the surface area of the nanotubes. The increased surface area enables more nanocrystals to be deposited on the TiO_2 nanotubes. Increasing the surface area of the nanotubes is one of the most efficient ways that enhance the solar cell efficiency because more nanocrystals on the nanotubes apparently generate more excited electrons. For the formation of a thin oxide layer at the interface, the use of a polar organic electrolyte is also essential. In this project, ethylene glycol was used as an organic electrolyte. It enables the minimization of the use of water content, allowing for a thinner oxide layer as well as the prevention of deteriorated tube structure resulting from an enhanced dissolution rate. For quantum dot sensitized solar cells, highly ordered free-standing nanotube structure is to be preferred due to the increased internal and external surface area and high carrier mobility with less recombination sites.

5.2.2 Crystalline Structure

The crystallinity of TiO_2 significantly affects the electronic properties and finally solar cell efficiency. The grown TiO_2 nanotube films were annealed at 400 ℃ and 500 ℃ respectively. As-formed TiO_2 film and annealed TiO_2 films were measured by XRD to characterize their crystal structure. The different crystallinity of the TiO_2 is observed in Figure 5.8.

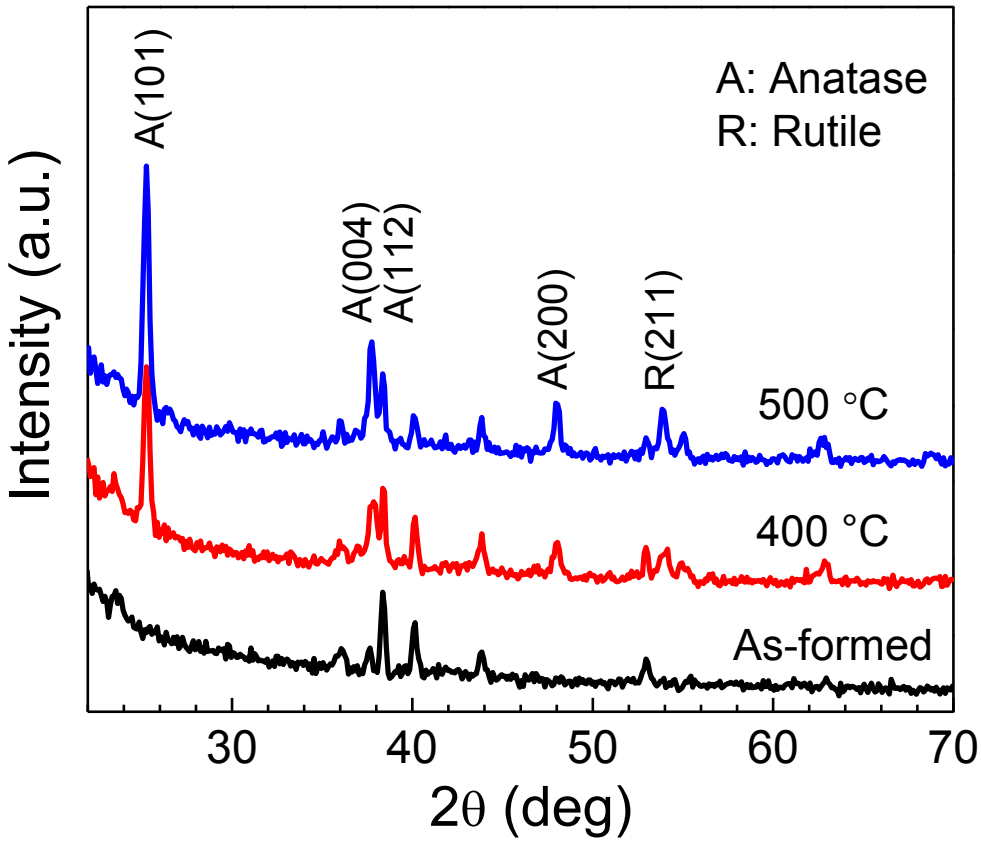

Figure 5.8 XRD patterns of a TiO_2 nanotube film annealed at different temperatures.

As-formed TiO_2 without annealing shows less structural information, which indicates the TiO_2 is amorphous. The TiO_2 annealed at 400 ℃ shows peaks of anatase and rutile, demonstrating the transformation of the amorphous into mixture of crystalline anatase and rutile. Further heating to 500 ℃ promotes the anatase crystallization, which is supported by the

increased intensity of anatase peaks. In contrast, there is no increase in the crystal formation of rutile. It was reported that annealing above 500 ℃ can lead to significant increase in rutile formation and at around 700 ℃ critical morphological deterioration such as sintering and collapse [25]. It is very important to convert amorphous to anatase form for photoelectric applications because anatase structure has a considerably higher charge carrier mobility than rutile. Therefore, the TiO_2 annealed at 500 ℃ is expected to have maximized anatase form and is optimized structure for solar cell fabrication.

5.3 Quantum Dot Sensitization

5.3.1 Layer-by-Layer Deposition

For the application of InP/ZnS nanocrystals in photovoltaic devices, the deposition experiment of InP/ZnS nanocrystals was performed. Self-assembled monolayer of thiol is a well-known linker to bond inorganic, organic materials to metal surfaces [56]. The sulfur atom connected to hydrocarbon chain confers specific properties to the surface of the nanocrystals and is used to anchor them. Layer-by-layer deposition of the nanocrystals using dithiol enables to build packed structure on glass. As the thickness of the nanocrystals increases, an increase in absorbance was detected in Figure 5.9.

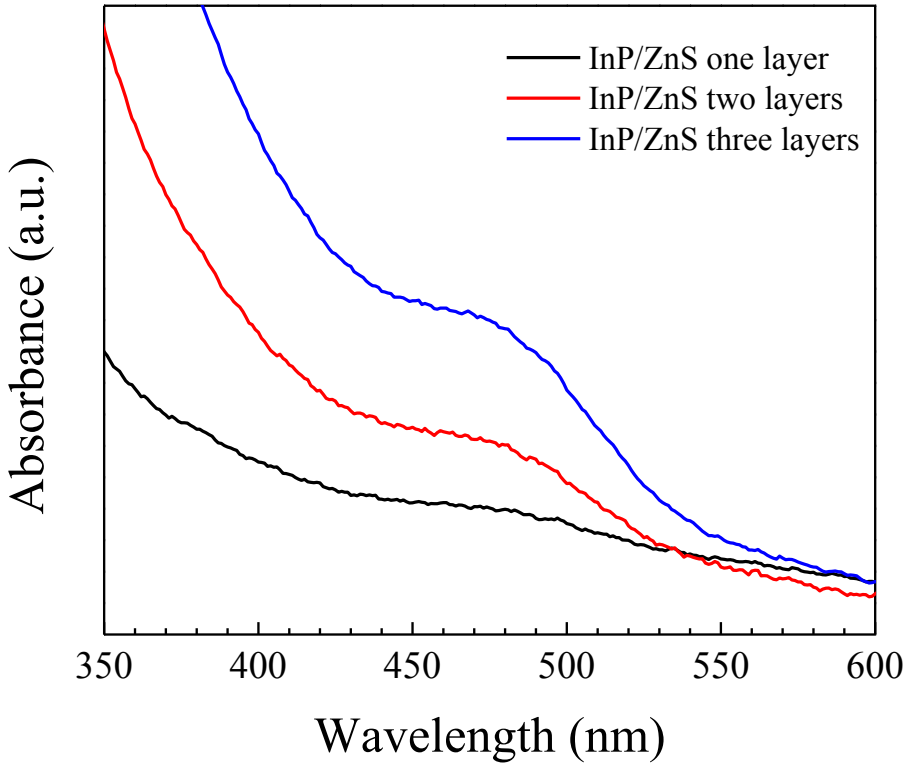

Figure 5.9 Absorbance spectra of InP/ZnS nanocrystals on glass by layer-by-layer deposition.

5.3.2 Electrophoretic Deposition

Coupling InP/ZnS nanocrystals with the TiO_2 free-standing nanotubes was carried out by using electrophoretic deposition method. This method is performed with two main controlling factors, which are suspension and process parameters. Particle size, dielectric constant of liquid, viscosity of suspension, and Zeta potential are suspension characteristics. The process parameters are applied voltage, deposition time, and the concentration of the colloidal solution. InP/ZnS nanocrystals grown for 120 min in one pot reaction were used, which determined the values of the suspension parameters. Therefore in this electrophoretic deposition experiment, applied voltage, deposition time, and the concentration of the InP/ZnS nanoparticles were considered as controllable parameters. 0.01 mg/ml of inP/ZnS nanoparticles in hexane was prepared as suspension. Dielectric constant of hexane, expressing the dissociating power of the solvent, is 1.89 at 20 ℃. The comparably low dielectric constant has a disadvantage because it limits the charge on the particles by low dissociation power. Insufficient charge on the particles to have reasonable moving force requires higher electric field strength. Deposition of the nanoparticles along the relatively long nanotubes is also in need of a higher electric field. The range of 1000 ~250 V/cm between two electrodes was applied to obtain an optimal and as high electric field as possible. Intensive evaporation of the hexane near the electrodes occurred at 1000 V/cm due to the heat generated by high current density. As electric field strength was decreased, evaporation was also diminished and was not observed at 250 V/cm. For stability and constant concentration of the suspension, the highest electric field 250 V/cm at which little evaporation occurs was determined for applied voltage. The reduction in the electric current as shown in Figure 5.10 indicates continuous deposition of the nanocrystals on the nanotubes.

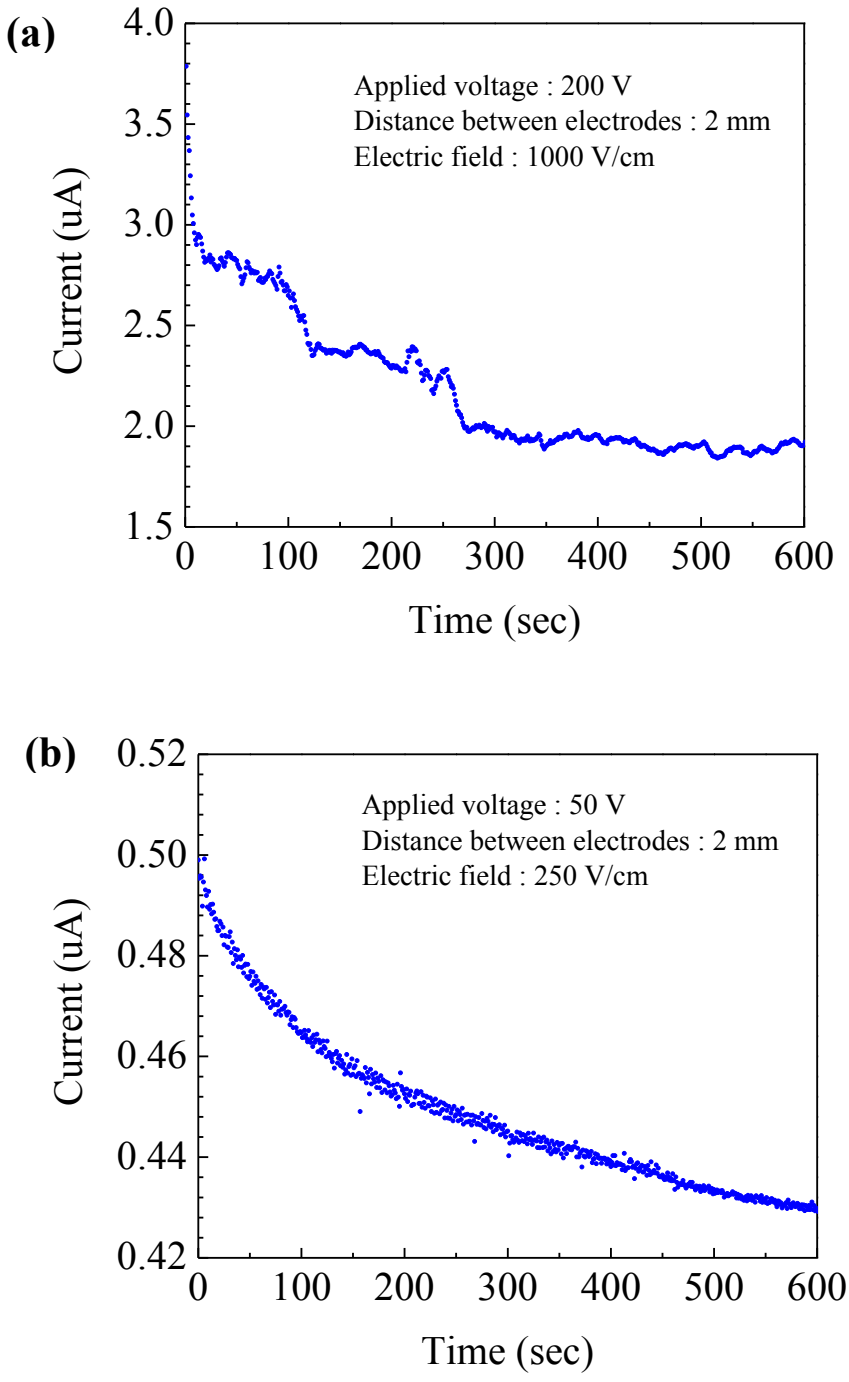

Figure 5.10 The current of electrophoretic deposition process with time at different electric field: (a) 1000 V/cm (b) 250 V/cm.

Yield of deposit is mainly associated with applied voltage between electrodes and deposition time. With the fixed electric field, deposition time can determine the deposit thickness of nanoparticles on the wall of the TiO_2 nanotubes. The weight (w) of particles per unit area of electrode can be calculated with the following equation used by Ishihara et al. [57] and Chen and Liu [58].

$$w = \frac{2}{3} C \cdot \varepsilon_0 \cdot \varepsilon_r \cdot \xi \cdot \left(\frac{1}{\eta}\right) \cdot \left(\frac{E}{L}\right) \cdot t \tag{5.1}$$

Where C is the concentration of the particle, $\boldsymbol{\varepsilon}_0$ is the permittivity of vacuum, $\boldsymbol{\varepsilon}_r$ is the relative permittivity of the solvent, ξ is the zeta potential of the particles, η is the viscosity of the solvent, E is the applied potential, L is the distance between two electrodes, and t is the deposition time. The velocity of a charged particle in a unit electric field is referred to as its electrophoretic mobility. The potential at the surface of shear, the limit of liquid moving with a charged particle, is termed zeta potential, which is related to the electrophoretic mobility by the Henry equation.

$$\mu \equiv \frac{v}{E} = \frac{2\varepsilon_0 \varepsilon_r \xi f(ka)}{3\eta} \tag{5.2}$$

Where μ is electrophoretic mobility, $f(ka)$ is Henry's function. The Debye length k is reciprocal length of an electrical double layer and the parameter a refers to the radius of the particle. In this experiment, the fact that InP/ZnS nanocrystals are small and suspended in low dielectric constant hexane allows $f(ka)$ to be 1.0 referred to as the Hückel approximation. For a simple calculation without measuring the zeta potential, μ can be obtained using the surface number Z, in units of elementary charge e described below [59].

$$\mu = \frac{Ze}{3\pi\eta d} \tag{5.3}$$

For InP/ZnS nanocrystals' mobility, average diameter $d = 5\ nm$ from the TEM image above and surface charge $Z = -0.1$ are used in Eq. (3). The relatively low surface charge approximation is attributed to the suspension at neutral resign. The mobility in hexane (η = 0.326 cP at 20°C) $\mu = -1.0 \times 10^{-5}$ cm^2 V^{-1} s^{-1} is obtained. From the Eq. (2) and mobility zeta potential $\xi = -29$ mV is obtained. The zeta potential represents that the surface potential assumption is very reasonable because typical zeta potential would be expected between $+30$ mV and -30 mV at pH values between 4 and 7.5. The weight (*w*) of particles per unit area can be expressed as a function of μ by using equation (2) and $f(ka) = 1$.

$$w = C \cdot \mu \cdot \left(\frac{E}{L}\right) \cdot t \tag{5.4}$$

By substituting the determined parameters, the concentration of the particle C = 0.01 g/cm3 and the electric field 250 V/cm, the relationship between deposition time and the deposit weight is obtained. In the experiment, the current between the two electrodes was measured as shown in Fig. 5.11 The reduction in the electric current as shown in the Figure indicates continuous deposition of the nanocrystals on the nanotubes. The approximate amount of the nanocrystal deposited on the nanotubes for 600 sec. 0.015 g/cm^2 is calculated from the Eq. (4). The well deposited nanoparticles on the nanotubes are observed in transmission electron microscopy (TEM) images of shown in Figure 5.11 before (a) and after (b) coupling the InP/ZnS nanocrystals.

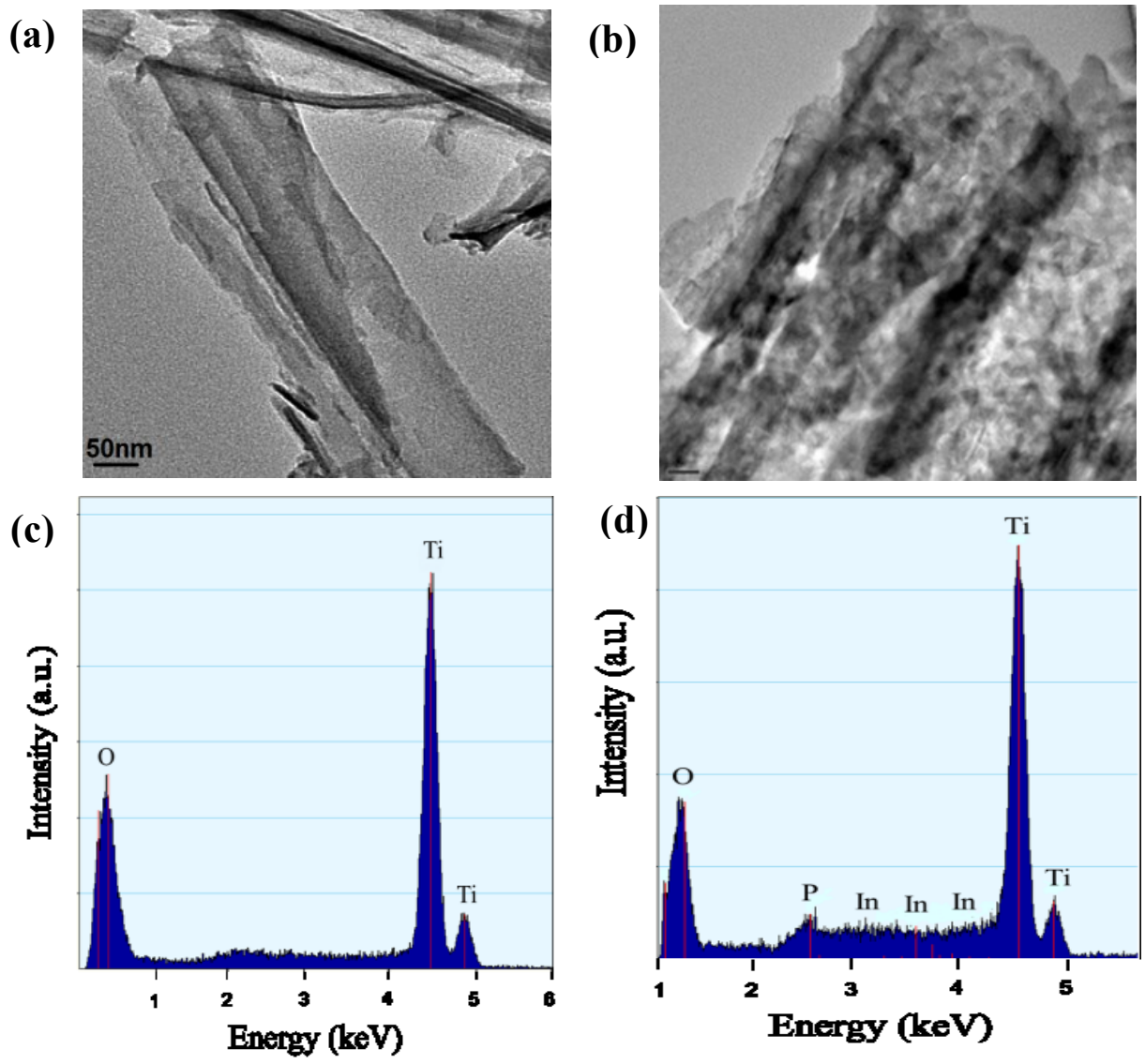

Figure 5.11 (a) TEM image shows the smooth wall of TiO_2 nanotubes before deposition. (b) The deposited InP/ZnS nanocrystals are distributed on the TiO_2 nanotubes in the TEM image. (c) EDX spectrum was taken from TiO_2 nanotubes corresponding to (b). (e) EDX spectrum was taken from TiO_2 nanotubes coupled with InP/ZnS nanocrystals corresponding to (c)

6. CONCLUSION AND FUTURE WORK

6.1 Conclusion

The synthesis of InP/ZnS nanocrystals has been investigated to obtain controlled size nanocrystals. The nanocrystals in the emission peak range of 520 nm to560 nm were synthesized by one pot reaction method. In order to increase InP core size to cover the wide range of visible region, InP core growth was separated from ZnS shell growth. As a result, a slight red-shift was observed. Preparation of indium precursor and the nanocrystal synthesis were performed subsequently *in situ*. This enabled InP core to grow larger, resulting from prevention of the InP surface passivation by oxidation. Very thin ZnS shell is estimated from the InP/ZnS nanocrystal TEM image. The very thin shell and close conduction band edges of InP and ZnS are expected to facilitate excited electrons in the InP conduction band readily to tunnel through the ZnS shell.

Free-standing TiO_2 nanotubes were grown on Ti foil by electrochemical anodization. By the control over the ratio between fluoride ions and deionized water, highly ordered TiO_2 nanotube arrays with tube diameter of 80 nm were obtained. Anatase crystal structure was obtained by annealing the as-grown TiO_2 nanotubes. The maximized anatase form improves crystallinity with high carrier mobility, which is expected to enhance the solar cell efficiency. The InP/ZnS nanocrystals were deposited on the TiO_2 nanotubes successfully by using electrophoretic deposition with the control over the distance between two electrodes and an applied voltage. Highly vertically ordered TiO_2 nanotubes coupled with broad spectrum InP/ZnS nanocrystals are expected to provide high efficient quantum dot sensitized solar cells.

6.2 Future Work

Fabrication of InP/ZnS nanocrystal sensitized TiO_2 solar cells will be carried out. TiO_2 nanotube geometric parameters, such as length, diameter, and type which strongly affect the solar cell performance, will be adjusted and the solar cell performance will be characterized. It is obvious the larger surface area TiO_2 nanotubes have the higher efficiency the solar cells are expected to have. This may be achieved by depositing TiO_2 nanoparticles on TiO_2 nanotubes, which is expected to increase surface area extremely. An electrolyte which transfers electrons from an electrode to sensitizers via oxidization and reduction is one of the crucial components in this solar cell. A redox electrolyte including iodide or sulfide which is most widely used in dye sensitized solar cells will be employed to measure the compatibility with InP/ZnS nanocrystals. All solid-state structure will be studied for the stability and durability of the solar cells.

When using an electrolyte, the counter electrode plays a significant role in the operation of solar cells. As a counter electrode, platinum is preferred due to the ability to catalyze the redox reaction especially in iodide electrolytes without being consumed. However, it is cost-prohibitive and not ideal for other electrolyte. Graphene is considered as a promising electrode because it is cost-effective, renewable, and environmentally friendly with advantages of extremely high conductivity and stability. Electrolyte and electrode affect each other, so that the study on these components will be carried out together for the compatibility and the performance of the devices.

REFERENCES

1. B. O'Regan, M. Grätzel, "A low cost, high-efficiency solar-cell based on dye-sensitized colloidal TiO_2 films," *Nature*, vol. 353, pp737-740, 1991.

2. M. Grätzel, "Photoelectrochemical cells," *Nature*, vol. 414, pp. 338-344, 2001.

3. M. Grätzel, A. Hagfeldt, "Molecular Photovoltaics," *Acc. Chem. Res.*, vol. 33, pp. 269-277, 2000.

4. L. Schmidt-Mende, S. M. Zakeeruddin, M. Grätzel, "Efficiency improvement in solid-state-dye-sensitized photovoltaics with an amphiphilic Ruthenium-dye," *Appl. Phys. Lett*., Vol. 86, pp. 013504, 2005.

5. I. Mazzarino, P. Piccinini, L. Spinelli, "Degradation of organic pollution in water by photochemical reactors," *Catal. Today*, vol. 48, pp. 315-321, 1999.

6. M. Kang, S. Y. Lee, C. H. Chung, S. M. Cho, G. Y. Han, B. W. Kim, K. J. Yoon, "Characterization of a TiO_2 photocatalyst synthesized by the solvothermal method and its catalytic performance for $CHCl_3$ decomposition," *J. Photochem. Photobiol. A*, vol. 144, pp. 185-191, 2001.

7. K. Zhu, N. R. Neale, A. Miedaner and A. J. Frank, "Enhanced Charge-Collection Efficiencies and Light Scattering in Dye-Sensitized Solar Cells Using Oriented TiO_2 Nanotubes Arrays," *Nano Lett*., vol. 7, pp. 69-74, 2009.

8. D. Kuang, P. Wang, S. Ito, S. M. Zakeeruddin and M. Grätzel, "Stable Mesoscopic Dye-Sensitized Solar Cells Based on Tetracyanoborate Ioinc Liquid Electrolyte," *J. Am. Chem. Soc*., vol. 128, pp. 7732-7733, 2006.

9. J. H. Yum, I. Jung, C. Baik, J. Ko, M. K. Nazeeruddin and M. Grätzel, "High efficient donor-acceptor ruthenium complex for dye-sensitized solar cell applications," *Energy Environ. Sci*., vol. 2, pp. 100-102, 2009.

10. M. K. Nazeeruddin, F. D. Angelis, S. Fantacci, A. Selloni, G. Viscardi, P. Liska, S. Ito, B. Takeru and M. Grätzel, "Combined experimental and DFT-TDDFT computational study of photoelectrochemical cell ruthenium sensitizers," *J. Am. Chem. Soc*., vol. 127, pp. 16835-16847, 2005.

11. A. Mishra, M. K. R. Fisher and P. Bäuerle, "Metal-free organic dyes for dye-sensitized solar cells: from structure property relationships to design rules," *Angew. Chem. Int. Ed.,* vol. 48, pp. 2474-2499, 2009.

12. J. Yan, F. Zhou, "TiO_2 nanotubes: structure optimization for solar cells," *J. Mater. Chem*., vol. 21, pp. 9406-9418, 2011.

13. R. Xie, D. Battaglia, and X. Peng, "Colloidal InP nanocrystals as efficient emitters covering blue to near-infrared," *J. Am. Chem. Soc*., vol. 129, pp. 15432-15433, 2007.

14. C. Burda, X. Chen, R. Narayanan, M. A. El-Sayed, "Chemistry and Properties of Nanocrystals of Different Shapes," *Chem. Rev*., vol. 105, pp. 1025-1102, 2005.

15. L. E. Brus, "Electron-electron and electron-hole interactions in small semiconductor crystallites: The size dependence of the lowest excited electronic state," *J. Chem. Phys*., vol. 80, pp. 4403-4409, 1984.

16. J. H. Yum, I. Jung, C. Baik, J. Ko, M. K. Nazeeruddin and M. Grätzel, "High efficient donor-acceptor ruthenium complex for dye-sensitized solar cell applications," *Energy Environ. Sci*., vol. 2, pp. 100-102, 2009.

17. Y. Paz, A. Heller, "Photo-oxidatively self-cleaning transparent titanium dioxide films on soda lime glass: The deleterious effect of sodium contamination and its prevention," *J. Mater. Res*., vol. 12, pp. 2759-2766, 1997.

18. V. Zwilling, E. Darque-Ceretti, A. Boutry-Forveille, D. David, M. Y. Perrin1 and M. Aucouturier, "Structure and physicochemistry of anodic oxide films on titanium and TA6V alloy," *Surf. Interface Anal.*, vol. 27, pp. 629-637, 1999.

19. D. Gong, C. A. Grimes, O. K. Varghese, W. Hu, R. S. Singh, Z. Chen, and E. C. Dickey, "Titanium oxide nanotube arrays prepared by anodic oxidation," *J. Mater. Res.,* vol. 16, pp. 3331-3334, 2001.

20. A. Ghicov, H. Tsuchiya, J. M. Macak and P. Schmuki, "Titanium oxide nanotubes prepared in phosphate electrolytes," *Electrochem. Commun*., vol. 7, pp. 505-509, 2005.

21. Y. Kim, C.H. Kim, Y. Lee and K. J. Kim, "Enhanced Performance of Dye-Sensitized TiO_2 Solar Cells Incorporating COOH-Functionalized Si Nanoparticles," *Chem. Mater*., vol. 22, pp. 207-211, 2010.

22. M. Grätzel, "Dye-sensitized solar cells," J. Photochem. Photobiol. C: Photochem. Rev., vol. 4. pp. 145-153, 2003.

23. M.K. Nazeeruddin, I. Kay, A. Rodicio, R. Humphry-Baker, E. Müller, P. Liska, N. Vlachopouloss, M. Grätzel, "Conversion of light to electricity by cis-X2bis(2,2'-bipyridyl-4,4'-dicarboxylate)ruthenium(II) charge-transfer sensitizers (X = Cl^-, Br^-, I^-, CN^-, and SCN^-) on nanocrystalline titanium dioxide electrodes," *J. Am. Chem. Soc.* vol. 115, pp. 6382-6390, 1993.

24. J. M. Macak, H. Tsuchiya, A. Ghicov and P. Schmuki, "Dye-sensitized anodic TiO_2 nanotubes," *Electrochem. Commun*., vol. 7, pp. 1133-1137, 2005.

25. A. Ghicov, P. Schmuki, "Self-ordering electrochemistry: a review on growth and functionality of TiO_2 nanotubes and other self-aligned MO_x structures," *Chem. Commun.,* pp. 2791-2808, 2009.

26. Y. L. Lee and Y. S. Lo, "Highly efficient Quantum-Dot-Sensitized Solar Cell Based on Co-Sensitization of CdS/CdSe," *Adv. Funct. Mater*., vol. 19, pp. 604-609, 2009.

27. H. J. Park, M. G. Kang, S. H. Ahn and L. J. Guo, "Facile route to polymer solar cells with optimum morphology applicable to roll-to-roll process," *Adv. Mater*., vol. 22, E247-E253, 2010.

28. K. Shankar, G. K. Mor, H. E. Prakasam, O. K. Varghese and C. A. Grimes, "Self-Assembled Hybrid Polymer-TiO_2 Nanotube Array Heterojunction Solar Cells," *Langmuir*, vol. 23, pp. 12445-12449, 2007.

29. S. Nakade, T. Kanzaki, Y. Wada, and S. Yanagida, "Stepped light-induced transient measurements of photocurrent and voltage in dye-sensitized solar cells: application for highly viscous electrolyte systems," *Langmuir,* vol. 21, pp. 10803–10807, 2005.

30. C. J. Liu, J. Olsen, D. R. Saunders, J. H. Wang. "Photoactivation of CdSe Films for Photoelectrochemical Cells," *J. Electrochem. Soc*., vol. 128, pp. 1224-1228, 1981.

31. Y. Ueno, H. Minoura, T. Nishikawa, M. Tsuiki. "Electrophoretically deposited CdS and CdSe anode for photoelectrochemical cells," *J. Electrochem. Soc.*, vol. 130, pp. 43-47, 1983.

32. J. H. Bang, P. V. Kamat, "Quantum Dot Sensitized Solar Cells. CdTe versus CdSe Nanocrystals," *ACS Nano.*, vol. 3, pp. 1467-1476, 2009.

33. I. Mora-Seró, S. Giménez, T. Moehl T, F. Fabregat-Santiago, T. Lana-Villareal, R. Gómez, and J. Bisquert, "Factors determining the photovoltaic performance of a CdSe quantum dot sensitized solar cell: the role of the linker molecule and of the counter electrode," *Nanotechnology*, vol. 19, pp. 424007 (7pp), 2008.

34. X. Peng, J. Wickham, A. P. Alivisatos, "Kinetics of II-V Colloidal Semiconductor Nanocrystal Growth: 'Focusing' of size distributions," *J. Am. Chem. Soc*., vol. 120, pp. 5343-5344, 1998.

35. B. R. Pamplin, *Crystal Growth*; Pergamon Press; New York, 1975.

36. J. Li and H. C. Zeng, "Hollowing Sn-Doped TiO_2 Nanospheres via Ostwald Ripening," *J. Am. Chem. Soc*., vol. 129, pp. 15839-15847, 2007.

37. Al. L. Efros, A. L. Efros, "Pioneering Effort I," in *Sov. Phys. Semicond*., vol. 16, pp. 772, 1982.

38. L. E. Brus, "A simple model for the ionization potential, electron affinity, and aqueous redox potentials of small semiconductor crystallites," *J. Chem. Phys*. vol. 79, pp. 5566-5571, 1983.

39. C. Yao and T. J. Webster, "Anodization: A Promising Nano-Modification Technique of Titanium Implants for Orthopedic Applications," *J. Nanosci. Nanotechno*., vol. 6, pp. 2682-2692, 2006.

40. G. E. Thompson, "Porous anodic alumina: fabrication, characterization and applications," *Thin Solid Films*, vol. 297, pp. 192-201, 1997.

41. V. P. Parkhutik and V. I. Shershulsky, "Theoretical modeling of porous oxide growth on aluminium," *J. Phys. D Appl. Phys*. vol. 25, pp. 1258-1263, 1992.

42. S. Bauer, S. Kleber, and P. Schmuki, "TiO_2 nanotubes: tailoring the geometry in H_3PO_4/HF electrolytes," *Electrochem. Commun.,* vol. 8, pp. 1321-1325, 2006.

43. J. M. Macak, H. Tsuchiya, A. Ghicov, K. Yasuda, R. Hahn, S. Bauer, and P. Schmuki, "TiO2 nanotubes: Self-organized electrochemical formation, properties and applications," *Curr. Opin. Solid State Mater. Sci.*, vol. 11, pp. 3-18, 2007.

44. G. K. Mor, K. Shankar, M. Paulose, O. K. Varghese, and C. A. Grimes, "Enhanced photocleavage of water using titania nanotube arrays," *Nano Lett*., vol. 5, pp. 191-195, 2005.

45. G. V. Samsonov (Ed) "*The Oxide Handbook*" 2nd Edn., IFI Plenum, New York-Washington, 1982.

46. O. O. Van der Biest, and L. J. Vandeperre, "Electrophoretic deposition of materials," *Annu. Rev. Mater. Sci*., vol. 29, pp. 327-352, 1999.

47. F. Grillon, D. Fayeulle, M. Jeandin, "Quantitative image-analysis of electrophoretic coatings," *J. Mater. Sci. Lett*., vol. 11, pp. 272-275, 1992.

48. Antonio Luque, and Steven Hegedus, *Handbook of Photovoltaic Science and Engineering*, Second Edition, Wiley and Sons, 2011.

49. M. Green, *Solar Cells: Operating Principles, Technology, and System Applications*. Englewood Cliffs, NJ: Prentice Hall, 1982.

50. R.W. Miles, K.M. Hynes, and I. Forbes, "Photovoltaic solar cells: An overview of state-of-the-art cell development and environmental issues", *Prog. in Cryst. Grow. and Charact. of Mat.*, vol. 51, pp. 1-42, 2005.

51. R. H. Bube, *Photovoltaic Materials*. London, UK: Imperial College Press, 1998.

52. L. Li and P. Reiss, "One-pot Synthesis of Highly Luminescent InP/ZnS Nanocrystals without Precursor Injection," *J. AM. Chem. Soc*., vol. 130, pp. 11588-11589, 2008.

53. W. K. Bae, K. Char, H. Hur and S. Lee, "Single-step synthesis of quantum dots with chemical composition gradients," *Chem. Mater*., vol. 20, pp. 531–539, 2008.

54. A. Cros-Gagneux, F. Delpech, C. Nayral, A. Cornejo, Y. Coppel, and B. Chaudret, "Surface Chemistry of InP Quantum Dots: A Comprehensive Study," *J. Am. Chem. Soc*., vol. 132, pp. 18147-18157, 2010.

55. D. Wang, Y. Liu, B. Yu, F. Zhou, and W. Liu, "TiO_2 nanotubes with tunable morphology, diameter, and length: Synthesis and photo-electrical/catalytic performance," *chem. Mater*., vol. 21, pp. 1198-1206, 2009.
56. D. G. Castner and B. D. Ratner, "Biomedical surface science: Foundations to frontiers," *Surface Science*, vol. 500, pp. 28-60, 2002.

57. T. Ishihara, K. Shimise, T. Kudo, H. Nishiguchi, T. Akbay, Y. Takita, "Preparation of Yttria-stabilized zirconia thin-films on strontium doped $LaMnO_3$ cathode substrate via electrophoretic deposition for solid oxide fuel cells," *J. Am. Ceram. Soc.,* vol. 83, pp. 1921-1927, 2000.

58. Chen F, Liu M, "Preparation of yttria-stabilized zirconia (YSZ) films on $La_{0.85}Sr_{0.15}MnO_3$(LSM) and LSM-YSZ substrate using an electrophoretic deposition (EPD) process," J. Eur. Ceram. Soc., vol. 21, pp. 127-134. 2001.

59. R. W. O'Brien, L. R. White, "Electrophoretic mobility of a spherical colloidal particle," *J. Chem. Soc. Farad. Trans. II,* vol. 74, pp.1607-1626, 1978.